

Key Points:

- Sediment transported in suspension is 3–4 times lower than sediment transported as bedload
- Sediment transported in suspension by mean currents is 2 orders of magnitude greater than sediment transported by waves
- Sea-swell waves typically transport sediment offshore and infragravity waves and mean currents typically transport sediment onshore

Correspondence to:

A. W. M. Pomeroy,
andrewpomeroy@gmail.com

Citation:

Pomeroy, A. W. M., Storlazzi, C. D., Rosenberger, K. J., Lowe, R. J., Hansen, J. E., & Buckley, M. L. (2021). The contribution of currents, sea-swell waves, and infragravity waves to suspended-sediment transport across a coral reef-lagoon system. *Journal of Geophysical Research: Oceans*, 126, e2020JC017010. <https://doi.org/10.1029/2020JC017010>

Received 24 NOV 2020
Accepted 9 FEB 2021

The Contribution of Currents, Sea-Swell Waves, and Infragravity Waves to Suspended-Sediment Transport Across a Coral Reef-Lagoon System

Andrew W. M. Pomeroy^{1,2,3} , Curt D. Storlazzi⁴ , Kurt J. Rosenberger⁴ , Ryan J. Lowe^{1,2,5} , Jeff E. Hansen^{2,5} , and Mark L. Buckley⁶ 

¹Oceans Graduate School, The University of Western Australia, Perth, WA, Australia, ²UWA Oceans Institute, The University of Western Australia, Perth, WA, Australia, ³Australian Institute of Marine Science, Perth, WA, Australia, ⁴U.S. Geological Survey, Pacific Coastal and Marine Science Center, Santa Cruz, CA, USA, ⁵School of Earth Science, The University of Western Australia, Perth, WA, Australia, ⁶U.S. Geological Survey, St. Petersburg Coastal and Marine Science Center, St. Petersburg, FL, USA

Abstract Coral reefs generate substantial volumes of carbonate sediment, which is redistributed throughout the reef-lagoon system. However, there is little understanding of the specific processes that transport this sediment produced on the outer portions of coral reefs throughout a reef-lagoon system. Furthermore, the separate contributions of currents, sea-swell waves, and infragravity waves to transport, which are all strongly influenced by the presence of a reef, is not fully understood. Here, we show that in reef-lagoon systems most suspended sediment is transported close to the seabed and can, at times, be suspended higher in the water column during oscillatory flow transitions (i.e., near slack flow) at sea-swell wave frequencies, and during the peak onshore oscillatory velocity phase at infragravity wave frequencies. While these wave frequencies contribute to the transport of suspended sediment offshore and onshore, respectively, the net flux is small. Mean currents are the primary transport mechanism and responsible for almost 2 orders of magnitude more suspended-sediment flux than sea-swell and infragravity waves. Whilst waves may not be the primary mechanism for the transport of sediment, our results suggest they are an important driver of sediment suspension from the seabed, as well as contributing to the partitioning of sediment grain sizes from the reef to the shoreline. As the ocean wave climate changes, sea level rises, and the composition of reef benthic communities change, the relative importance of mean currents, sea-swell waves, and infragravity waves is likely to change, and this will affect how sediment is redistributed throughout reef-lagoon systems.

Plain Language Summary Most of the sandy sediment found on coral reef coastlines is produced by organisms living within the reef. This sediment is then transported by waves and currents across the reef and distributed throughout the lagoon. Little is known about these transport processes, including the relative importance of how currents or different types of waves drive transport. This study shows that most of the sediment in the water column (suspended sediment) is transported close to the seabed by mean currents. At times, this sediment can be suspended higher in the water column by short waves (5–25 s) when the flow transitions from being onshore directed to offshore directed, or when the velocities of longer period waves (25–250 s), called infragravity waves, are directed onshore. The timing of the suspension by these waves helps to sort the sediment into different sizes across the system, but the quantity of sediment transported is small. As the ocean wave climate changes, sea level rises, and reefs change, the relative importance of mean currents, sea-swell waves, and infragravity waves is also likely to change, and this will affect how sediment is redistributed throughout reef-lagoon systems. This study provides insight into what changes may be expected.

1. Introduction

Tropical beaches protect and support communities of hundreds of millions of people globally (Hoegh-Guldberg et al., 2019). These beaches are primarily accumulations of sediment derived from the calcium carbonate skeletal remains of organisms such as coral, crustose coralline algae, and mollusks from adjacent coral reefs (Perry & Hepburn, 2008). When these skeletal remains break down into particle sizes that can

be mobilized and transported by waves and currents, they are redistributed and deposited on the adjacent shoreline (e.g., Perry et al., 2011; Sanderson & Eliot, 1996; Woodroffe et al., 1999), on other parts of the reef substrate (e.g., Harney & Fletcher, 2003; Storlazzi et al., 2009), in nearby lagoons (e.g., Kench, 1998b; Kennedy & Woodroffe, 2000), or are exported via channels and breaks in the reef into deeper water (e.g., Hine et al., 1981; Hughes, 1999; Storlazzi et al., 2004). The ability to accurately predict sediment transport rates and patterns throughout a reef environment is essential to forecast how tropical beaches may be affected by changes in storminess, sea level, coral reef health, as well as for the design of interventions such as reef restoration.

The morphology of a coral reef environment affects the hydrodynamics over the reef, in the lagoon, and at the shoreline. The steep fore reef slope and shallow reef flat transforms and dissipates the incident open-ocean wind wave energy through depth-limited wave breaking and bottom friction (Lowe et al., 2005; Monismith et al., 2013). Some of the incident wave energy in the sea-swell frequency-band (“SS”, >0.04 Hz) that is not dissipated at the reef crest continues to propagate over the reef flat (e.g., Gourlay, 1994; Hardy & Young, 1996) and can also generate undular bore trains (Demirbilek et al., 2007; Gallagher, 1972; Sous et al., 2019). A proportion of the incident energy is also transferred to lower frequencies, such as the infragravity (“IG”, 0.004–0.04 Hz) wave band (Péquignet et al., 2014; Pomeroy, Lowe, et al., 2012; Symonds et al., 1982) or even a longer very low frequency band (“VLF”, <0.004 Hz). This redistribution of wave energy to lower frequencies can become a large proportion of the total wave energy in reef environments (e.g., Brander et al., 2004; Cheriton et al., 2016; Hardy & Young, 1996; Lugo-Fernández et al., 1998; Péquignet et al., 2009; Pomeroy, Lowe, et al., 2012; Roeber & Bricker, 2015), can resonate under specific conditions (Gawehn et al., 2016; Péquignet et al., 2009; Pomeroy et al., 2012) as well as form nonlinear bores that propagate across the reef toward the shoreline (Cheriton et al., 2020).

As incident SS waves shoal and break on the fore reef slope or reef crest, radiation-stress gradients are generated that are primarily balanced by a combination of wave-induced setup on the reef flat (Becker et al., 2014; Buckley et al., 2015, 2016; Longuet-Higgins & Stewart, 1964) and mean bottom stresses that are associated with wave-averaged cross-reef currents that are driven by the cross-reef pressure gradients (e.g., Coronado et al., 2007; Gourlay, 1996a, 1996b; Hench et al., 2008; Jago et al., 2007; Lowe et al., 2009a; Massel & Gourlay, 2000; Monismith et al., 2013; Taebi et al., 2011). The magnitude of this current depends on the water depth on the reef, the bottom roughness, and the reef morphology such as the reef flat width, lagoon depth, and the configurations of breaks in the reef (e.g., Gourlay & Colleter, 2005; Hearn, 1999; Lowe et al., 2009b; Pomeroy et al., 2018; Symonds et al., 1995). In addition to these SS, IG, and VLF waves, locally generated wind waves can also make an important contribution to the reef hydrodynamics (e.g., Cuttler et al., 2018; Pomeroy et al., 2018). Thus, in contrast to many open coast beaches, the hydrodynamics that define a reef-lagoon system are often defined by a bi-modal wave spectrum that is characterized by high- and low-frequency wave energy combined with mean cross-reef currents.

Most studies of sediment transport in coral reef environments have focused on the physical processes that drive suspended-sediment concentration (SSC) variability. These studies have typically evaluated the relative importance of SS waves and currents and how these contributions are affected by water depth, usually through direct correlation between SSC and bed shear stress (e.g., Harris et al., 2014; Kench, 1998b; Ogston et al., 2004; Pomeroy et al., 2018; Storlazzi et al., 2004; Suhayda & Roberts, 1977; Vila-Concejo et al., 2014). In general, these studies suggest that most sediment is suspended from the seabed by the stress imposed on the sediment by SS waves, and once suspended the sediment is transported by currents. Waves seem to be especially important in back-reef and lagoon areas where the sediment is typically sand size (e.g., Kench, 1998a; Morgan & Kench, 2014, 2016) and currents are often slower than on the reef flat (e.g., Pomeroy et al., 2018; Presto et al., 2006; Storlazzi et al., 2009; Taebi et al., 2011). It is worth noting that many studies estimate the critical shear stress based on bed sediment composition analogous to beaches and rivers, which in reef environments may not always be related to the sediment in suspension (Pomeroy et al., 2017; Storlazzi et al., 2010). Few studies have quantified the contribution—if any—of IG waves to sediment transport processes, either explicitly or through the careful choice of bulk spectral parameters. Laboratory experiments suggest that IG waves may make an important contribution to cross-reef sediment transport (Pomeroy et al., 2015); however, results from field experiments so far have been less definitive (Pomeroy et al., 2018). Importantly, a key limitation of almost all of these studies is that they rely on point

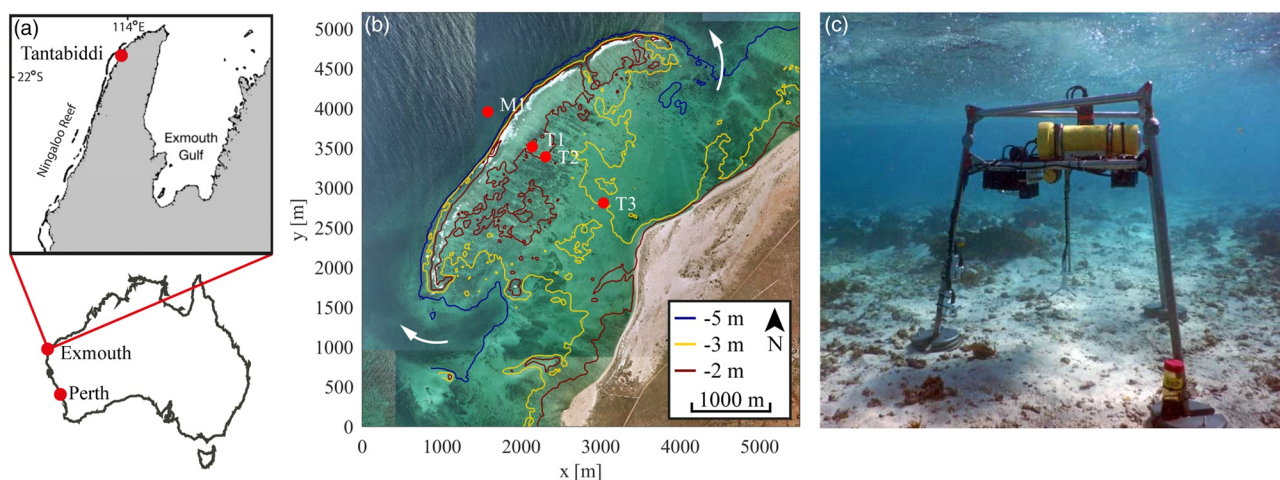


Figure 1. Overview of the Ningaloo Reef field site at Tantabiddi. (a) The location of the study site at Ningaloo Reef, which is ~32 km from the regional center of Exmouth (by road). (b) The location of the four instrument packages, with the acoustic Doppler directional wave gauge/current profiler at M1 on the fore reef and the cross-reef tripods at T1–T3. The depth contours at the site are shown and the white arrows indicate the channels and breaks in the reef. (c) Photograph of tripod T2 (Curt Storlazzi, USGS). Each tripod contained an acoustic Doppler profiler, an acoustic Doppler velocimeter, two optical backscatter sensors, and three sonar altimeters.

measurements at some distance from the seabed. How SSC varies throughout the water column in coral reef environments, the extent to which this SSC distribution is spatially and frequency dependent, and the overall importance of suspended-sediment flux (SSF) in comparison to bedload transport has not been fully quantified.

The aim of this study was to (a) quantify the magnitude and distribution of sediment in the water column at different locations and elevations above the seabed in a coral reef-lagoon system, (b) determine how this magnitude and distribution changes due to differences in SS and IG forcing, and (c) quantify the magnitude and direction of the resultant SSF. In Section 2, we first describe a field experiment that focuses on a fringing reef in north-western Australia, including the instrument configurations and the data analysis methods. The results are then presented in Section 3. In Section 4, we discuss the relative importance of SSF and bedload transport to the magnitude of sediment transport across the reef platform. Finally, we consider the implications of the spatial and temporal variability in both the hydrodynamics and SSC for different zones across the reef.

2. Methods

2.1. Study Design

We analyzed four subsets of data collected along a cross-reef transect during the MegaReef 2016 experiment. The MegaReef experiment was a 4-week field experiment conducted from 24 May to 21 June 2016 where ~90 instruments were deployed throughout a fringing reef-lagoon system in northwestern Australia. In that field experiment, data were collected spatially and vertically through the water column across the reef and lagoon. Combined with bedform migration measurements (Rosenberger et al., 2020), these data provide a unique opportunity to quantify cross-reef hydrodynamics and SSC, as well as to determine the relative contribution of both SSF and bedload to the total sediment flux.

2.2. Site Description

The field site located at Ningaloo Reef (Figure 1a) near Tantabiddi (21°5206.03"S, 113°58058.26"E; Figure 1b) has been described in detail by Pomeroy et al. (2018) and Cuttler et al. (2019), and is only summarized here. The reef crest is located 2.0–2.5 km from the shoreline with a reef flat that is ~0.6–1.5 m below mean sea level at still water and is ~500 m in width. The lagoon is generally ~3 m deep with channels that are up to ~6 m deep that cut into the reef flat and reef crest to the north and south. The mean currents are

Table 1
Instrument Site Information and Sampling Configuration

Site	Depth ^a (m)	Instrumentation	Sampling regime ^b
M1 (fore reef)	~18	Nortek AWAC	1 Hz with 2,048 s burst every 3,600 s current profile every 5 min
		RBR Virtuoso D	Continuous at 1 Hz
T1 (outer reef flat)	~2.4	Nortek ADP-HR	1 Hz continuous, downward facing with 2.5 cm bins
T2 (inner reef flat) ^c	~2.3	Nortek ADV	8 Hz with 14,400 samples every 3,600 s at 0.2 mab
T3 (lagoon)	~3.4	Seapoint OBS	8 Hz with 14,400 samples every 3,600 s at 0.2 mab
		Echologger AA400 Altimeters	1 Hz with 3,600 samples every 3,600 s at 0.4 mab 2 Hz with 20 samples every 600 s at 0.87 mab

^aDepth is relative to mean sea level. ^bMeasurement elevations are in meters above the seabed (mab). ^cADV velocity measurements were not obtained due to an instrument fault.

predominantly defined by subtidal variations in the offshore incident wave conditions and are driven across the reef flat to the lagoon, where the flow diverges toward the adjacent channels (Pomeroy et al., 2018). In addition to the subtidal variability, mean currents within the lagoon also vary at intratidal timescales due to tidal modulation of the wave-driven flows (Pomeroy et al., 2018). The spatial distribution of sediment at the site generally follows the mean current patterns, with the coarsest material on the outer reef flat, and finer material within the lagoon (Cuttler et al., 2019).

2.3. Field Measurements

The subset of data used in our study consisted of wave data that were measured on the fore reef at M1 with an acoustic Doppler directional wave gauge/current profiler (AWAC) and the three identical instrument tripods that were deployed along a cross-reef transect (Figures 1b and 1c). The instruments on each tripod (Table 1) included a downward-facing acoustic Doppler profiler (ADP) that measured the velocity profile, a downward-facing acoustic Doppler velocimeter (ADV), two optical backscatter sensors (OBS), and a set of three downward-facing altimeters spaced 6.5 cm apart horizontally in a cross-shore orientation. The time-averaged characteristics of the sediment in suspension were determined from sediment samples obtained in a sediment trap ($\varnothing = 75$ mm, height = 200 mm) positioned 0.2 m above the bed. A meteorological station was deployed on the shore adjacent to the site and recorded wind speed, direction, and barometric pressure.

2.4. Hydrodynamic Data Analysis

The offshore incident wave height ($H_{m0,ic}$), peak wave period (T_p), and peak wave direction (θ_w), were determined from the fore reef AWAC (M1) for each burst of data. On the reef flat and in the lagoon, one-dimensional surface elevation spectra were derived from the pressure time series at each tripod, which was converted to surface elevation using linear wave theory. From each spectra, the hourly root mean squared (RMS) wave heights for the shorter-period (5–25 s) SS waves ($H_{RMS,SS}$) and longer period (25–250 s) IG waves ($H_{RMS,IG}$) were calculated.

The raw ADV and ADP velocity (u) data were filtered to remove velocity spikes (e.g., caused by bubbles or debris in the sample volume) using a kernel-based despiking algorithm (Goring & Nikora, 2002). For each hourly burst of data, the depth-averaged mean current speed (U) and direction (θ_m) were computed. The mean current vector was then removed from the data and the local direction of wave propagation was determined via a covariance analysis; the angle of rotation required to orient the (residual) east and north components of oscillatory velocity data (\tilde{u}_E, \tilde{u}_N) into a coordinate system defined by the maximum and minimum variance. For the ADP, the angle of rotation was determined from the average of the bottom 10 valid bins in the profile. We defined the lowest valid bin as the bin elevation with the highest acoustic backscatter, which we averaged across all three beams for each time step, less one standard deviation of the distance to

the bin with the highest acoustic backscatter. This typically resulted in the exclusion of the bin at the top of the mobile sediment layer (verified from measurements of the deployed instruments) and the bin immediately above it. We then removed an additional bin to eliminate data that may be affected by acoustic sidelobe interference with the bed. We validated our assessment technique with the position of the bed calculated from the altimeter data.

2.5. Sediment Grain-Size Distributions

To determine the grain size distribution of the sediment on the seabed as well as in suspension, we compared seabed sediment samples with the sediment trap samples at the end of the experiment. The bed sediment samples were obtained from the top ~5–7 cm in the center of each tripod prior to tripod deployment. The grain-size distribution of each sample was determined using a Beckman LS-13-320 laser diffraction particle size analyzer and the percentages of calcium carbonate and terrigenous determined following the methods described by Barber (2002).

We compared the sediment distributions to the grain size (D) predicted to be suspended by the hydrodynamics at each site. First, we calculated shear velocities (u_*) imposed on the bed by mean currents (u_{*M}), SS waves (u_{*SS}) and IG waves (u_{*IG}) waves. Note that we chose to limit this study to these components, which were clearly apparent in the wave spectra, VLF motions were not considered. As the instrument tripods were deployed on reasonably flat sections of the reef and lagoon, the immediate influence of roughness elements (e.g., coral) on the flow was minimal. For T1 and T3, we used the 8 Hz ADV data, while at T2, where the ADV failed, we used the ADP data from the cell located at the elevation of the ADV to maintain consistency.

It is important to make a distinction at this point. The total resistance experienced by the overlying flow that is responsible for hydrodynamic transformations and dissipation can be partitioned into two components: (1) a bed stress component that is due to the stress imposed by sediment grains at the bed and (2) a form drag component that is due to drag forces either by mobile bed forms (e.g., due to ripples, which we show later can be present at this site) or by immobile roughness (e.g., coral assemblages). In this study, we principally focus on the mobilization of sediment from the bed and thus focus on the calculation of the bed stress component, which in reef environments can be much smaller than the total resistance and is located within the roughness layer that develops due to the presence of large roughness elements (Pomeroy et al., 2017). We note, however, that organized structures such as vortices that develop along with the form drag component can be important for the diffusion of sediment higher in water column.

To estimate the u_* imposed on the sediment, we adopted the approach proposed by Soulsby and Clarke (2005) as adapted by Malarkey and Davies (2012). From the wave velocity spectra, we calculated a representative orbital velocity (u_r) and representative frequency (f_r):

$$u_r = \sqrt{2 \sum_i S_{\tilde{u}_E \tilde{u}_N, i} \Delta f_i} \quad (1a)$$

$$f_r = \frac{\sum_i f_i S_{\tilde{u}_E \tilde{u}_N, i} \Delta f_i}{\sum_i S_{\tilde{u}_E \tilde{u}_N, i} \Delta f_i} \quad (1b)$$

where $S_{\tilde{u}_E \tilde{u}_N} = S_{\tilde{u}_E \tilde{u}_E} + S_{\tilde{u}_N \tilde{u}_N}$ is the combined horizontal velocity spectrum and “~” denotes the oscillatory (unsteady) component. In our approach, the current-alone drag coefficient was calculated based on the assumption that a logarithmic profile develops within the unresolved region between the seabed and our lowest hydrodynamic measurement:

$$C_D = \left(\frac{\kappa}{\log \left(\frac{z-d}{z_0} \right) - 1} \right)^2 \quad (2a)$$

where κ is the von Karman constant (0.4), z is the height above the seabed up to the limit of our lowest valid velocity measurement, and d is the mean velocity profile displacement, which close to the seabed is approximately zero, and $z_0 = D_{50} / 12$, with D_{50} the median grain size of the suspended sediment trap distribution. The wave friction coefficient (f_w) was calculated using the formulation proposed by Soulsby et al. (1993):

$$f_w = 1.39 \left(\frac{A}{z_0} \right)^{-0.52} \quad (2b)$$

where A is the semi-orbital excursion for the representative wave conditions ($u_r / f_r 2\pi$). Implicit in this assumption is that the representative hydraulic roughness length (z_0) is constant and applicable across different wave frequencies. Based on laboratory and field observations, this assumption is reasonable (Lowe et al., 2005; Mathisen & Madsen, 1999). However, the choice of roughness formulation is unlikely to change the interpretation of results.

Next, to relate the suspended sediment grain size distribution to u_* , we determined the equivalent sediment diameter D that could be suspended by a given shear velocity based on the downward particle fall velocity (w_s). Following Pomeroy et al. (2017), we assumed that the shear velocity that mobilizes the sediment grains into suspension is directly related to the fall velocity of the sediment grains (i.e., $u_* = w_s$); once these grains are mobilized, they directly enter a state of suspension. Whether sediment was in a burst or fully developed suspension is not relevant for this analysis. We used the Soulsby (1997) formulation to estimate w_s as:

$$w_s = \frac{\nu}{D} \left(\sqrt{10.36^2 + 1.049 D_*^3} - 10.36 \right) \quad (3)$$

where ν is the kinematic viscosity of water ($9.35 \times 10^{-7} \text{ m}^2 \text{ s}^{-1}$) and D_* is the dimensionless grain size ($D_* = \left(g(s-1) / \nu^2 \right)^{1/3} D$) with g being the gravitational acceleration constant and s the ratio of sediment grain density (ρ_s) to water density (ρ_w). Rosenberger et al. (2020) reported that ρ_s varied along the transect and was smaller than those reported by Cuttler et al. (2015). For simplicity, in Equation 3, we used the average of the measurements reported by Rosenberger et al. (2020), which were also obtained for this specific experiment ($\rho_s = 2167 \text{ kg m}^{-3}$).

2.6. Backscatter Calibration

The OBS data were postcalibrated in the laboratory using the sediment that was collected in the traps positioned above the bed. We used a 60 L resuspension tank to which we added known quantities of trap sediment. As each sample was added to the tank, we measured the optical backscatter for 5 min prior to taking a sample of the water and sediment to verify the actual concentration relative to the predicted concentration. Each sample was vacuum filtered onto preweighed glass fiber filter (Whatman GF/C, 0.8 μm), dried (75°C for 24 h), and weighed in order to calculate SSC. The known SSCs obtained through filtration were related via linear regression to the measured optical backscatter time-averaged over the 5 min tank sampling duration.

To calibrate the ADV and ADP acoustic backscatter (ABS), we related the time-averaged SSC from the calibrated lower and upper OBSs to the ABS. For the ADV, we directly related the ADV ABS to the lower OBS, as these instruments were approximately co-located. The ADP ABS data were first corrected for acoustic decay over distance in water (e.g., Ha et al., 2011), before three measurement bins centered on the height of each OBS were averaged at each time step. A linear equation was then fit to the data. The variability in the SSC magnitude from the ADV ABS, OBS, and ADP ABS was similar between instruments at each location, but the ADP ABS often exhibited a slightly lower SSC than the OBS and ADV ABS, during the larger swell events. We chose not to use the OBS data for the subsequent concentration or flux analysis, as they were point sources and typically showed evidence of biofouling later in the experiment.

Table 2
The Representative Forcing Conditions for Selected 3 h Bursts of Data

Case	Definition	$H_{RMS,IG}$ (m)	$H_{RMS,SS}$ (m)	$H_{RMS,IG}/H_{RMS,SS}$ (-)	N_{IG} (-)	N_{SS} (-)
$\downarrow_{IG}\downarrow_{SS}$	Low $H_{RMS,IG}$, Low $H_{RMS,SS}$	0.13	0.11	1.2	254	1,315
$\downarrow_{IG}\uparrow_{SS}$	Low $H_{RMS,IG}$, High $H_{RMS,SS}$	0.08	0.34	0.2	277	1,241
$\uparrow_{IG}\downarrow_{SS}$	High $H_{RMS,IG}$, Low $H_{RMS,SS}$	0.19	0.11	1.8	270	1,276
$\uparrow_{IG}\uparrow_{SS}$	High $H_{RMS,IG}$, High $H_{RMS,SS}$	0.17	0.30	0.6	284	1,287

Note. The root-mean-squared sea-swell ($H_{RMS,SS}$) and infragravity ($H_{RMS,IG}$) wave heights on the reef flat at T1 for the representative cases are shown along with the number of sea-swell (N_{SS}) and infragravity (N_{IG}) wave ensembles used for the ensemble averaging.

2.7. Suspended-Sediment Flux (SSF)

The u and SSC (c) series data derived from the ADP were decomposed into mean (steady) and oscillatory (unsteady) components at each elevation where data were obtained via:

$$\langle uc \rangle = \langle (\bar{u} + \tilde{u})(\bar{c} + \tilde{c}) \rangle = \underbrace{\bar{u}\bar{c}}_{Q_M} + \langle \tilde{u}\tilde{c} \rangle \quad (3a)$$

where $\langle \rangle$ denotes time-averaging over the hourly burst of data and the overbar indicates mean quantities. The first term on the right-hand side of Equation 3a is the SSF driven by the mean (wave-averaged) Eulerian flow (Q_M). The second term is the oscillatory flux and is nonzero when fluctuations in velocity and SSC are correlated. The cross-terms are zero by definition. The oscillatory component was further decomposed into its SS and IG contributions, corresponding to the first two terms on the right-hand side of Equation 3b, respectively:

$$\langle \tilde{u}\tilde{c} \rangle = \langle (\tilde{u}_{SS} + \tilde{u}_{IG})(\tilde{c}_{SS} + \tilde{c}_{IG}) \rangle = \underbrace{\langle \tilde{u}_{SS}\tilde{c}_{SS} \rangle}_{Q_{SS}} + \underbrace{\langle \tilde{u}_{IG}\tilde{c}_{IG} \rangle}_{Q_{IG}} + \langle \tilde{u}_{SS} + \tilde{c}_{IG} \rangle + \langle \tilde{u}_{IG} + \tilde{c}_{SS} \rangle \quad (3b)$$

The cross-product terms (the last two terms in Equation 3b) represent interactions between SS and IG oscillations, which were uncorrelated and at least 2 orders of magnitude smaller than the other terms.

We note that the wave and current velocity was predominantly cross-shore directed except for the occasional burst of data when the incident wave forcing and reef flat water depth were small, which resulted in an increased alongshore current component at T3 as the flow diverged toward the channels and breaks in the reef (Figure 1b). To determine the cumulative SSF over the experiment in the lowest 0.5 m of the water column, we vertically integrated each SSF component (Q_M , Q_{SS} , and Q_{IG}) at each location.

2.8. Phase-Averaged Quantities

To evaluate how the SSC and SSF varied due to differences in SS and IG energy vertically within the water column as well as throughout a wave cycle, at each location we calculated the ensemble average of u and c at each phase for four different forcing conditions (Table 2). For each forcing condition, we first identified individual waves using a zero downcrossing analysis of the demeaned and band-pass filtered SS and IG velocity data and extracted the u and c for each wave to form an ensemble. As the band-passing of the concentration data resulted in a zero mean, for each wave we set the largest negative concentration to be 0 mg L^{-1} and rescaled the concentration to better represent the relative increase and decrease in concentration. The u , c , and Q were then normalized for each wave phase (t/T):

$$X(t/T) = \frac{1}{N} \sum_{n=0}^{N-1} X(t + nT) \quad (4)$$

where X represents some quantity over time and N is the number of ensembles. This ensemble-averaged approach enabled greater statistical confidence in the data for each condition whilst also accommodating variability in the data due to the irregular forcing conditions.

3. Results

3.1. Forcing

The winds recorded during the experiment were light to moderate ($0\text{--}10\text{ m s}^{-1}$) and were typically onshore or obliquely onshore (Figure 2a); a diurnal sea breeze was prevalent during the latter part of the study period. The tidal range varied from 0.21 to 1.56 m (Figure 2b). The $H_{m0,ic}$ measured on the fore reef at M1 ranged from 0.53 to 2.79 m, with a mean (μ) height of 1.27 m and a standard deviation (σ) of 0.44 m (Figure 2c). These waves had a T_p of 5–24 s ($\mu = 14$ s), and generally approached the reef with a θ_w of between 230° and 275° ($80^\circ\text{--}40^\circ$ off the cross-reef direction). During the experiment, four swell events were measured (Figures 2c and 2d). The largest event (#1, Figure 2c) where $H_{m0,ic} = 2.79$ m, occurred 29–31 May as the tide approached its neap phase. The other large event (#4 where $H_{m0,ic} = 2.53$ m, Figure 2c) occurred during the spring phase of the tide from 6 to 9 June. Between these events, two smaller swell events occurred where $H_{m0,ic} = 2.20$ and 2.26 m, respectively.

3.2. Reef-Lagoon Hydrodynamics

A large reduction in the SS wave heights was observed on the outer reef flat near the crest at T1 (Figure 3a), located ~ 350 m shoreward of the surf zone, with $H_{RMS,SS}$ ranging from 0.05 to 0.6 m ($\mu = 0.29$ m). Farther toward shore, on the inner reef flat (T2) and inside the lagoon (T3), the SS heights continued to decrease; the mean $H_{RMS,SS}$ at T3 was reduced by on average 20% when compared to T1 (Figures 3b and 3c). Within the reef, the SS wave heights were strongly modulated by tidal changes in reef flat water depth, which affected the height of the waves that could propagate over the reef and toward the shoreline.

The $H_{RMS,IG}$ on the outer reef flat at T1 were generally smaller (range: 0.04–0.22 m, $\mu = 0.09$ m) than the corresponding SS wave heights (Figure 3a). However, when reef flat depths became shallow at low tide or when incident SS wave heights offshore were relatively large, such as during larger swell events (e.g., 30 May), $H_{RMS,IG}$ increased substantially. During these events, there was also a substantial increase in the depth-averaged mean current speeds U (Figure 3b), which could be as high as $\sim 0.2\text{--}0.4\text{ m s}^{-1}$. The $H_{RMS,IG}$ gradually decayed over the reef flat toward the inner reef flat (T2) and in the lagoon (T3). This decay was slightly less (15%) than the SS waves (Figures 3b and 3c). Like $H_{RMS,SS}$, both $H_{RMS,IG}$ and the U were also tidally modulated. The wave spectra reveal that the IG motions predominantly occur during these swell events with some dissipation across the instrument transect (Figures 3d–3f).

3.3. Grain Size Distributions

The grain size distribution of the seabed sediment obtained at each site was predominantly sand-sized (0.063–2 mm) and almost entirely composed of calcium carbonate (e.g., Figure 4 and Table 3). The presence of gravel-sized grains of shell hash decreased in size and quantity toward the shoreline. The peak grain size as a percentage by mass was similar on the reef flat at T1 and T2 (0.84 mm) but slightly finer in the lagoon at T3 (0.5 mm). The sediment collected in the traps at the elevation of the lower ADV and OBS was finer than the bed sediment collected at the same site and did not contain gravel-sized grains of shell hash that were observed in the bed samples. At T1 on the outer reef flat, the peak grain size as a percentage by mass of the trap sediment distribution was similar to the peak in the bed sediment (0.7 mm), but this peak grain size became progressively finer than the bed sediment across the site (T2 = 0.59 mm and T3 = 0.21 mm).

Estimation of the sediment grain size (D) that could be suspended into the water column at each site indicates that largest D were associated with the shear stress contribution from the SS waves (Figure 5). Despite these SS waves being depth-limited on the reef flat and thus relatively small (<0.5 m), the D estimated from u_{*SS} was $\sim 2\text{--}3$ times greater than the D estimated by u_{*IG} or u_{*M} . Mean currents and IG waves alone typically suspended sediment with smaller D (<0.15 mm), except during the events when the estimated D was

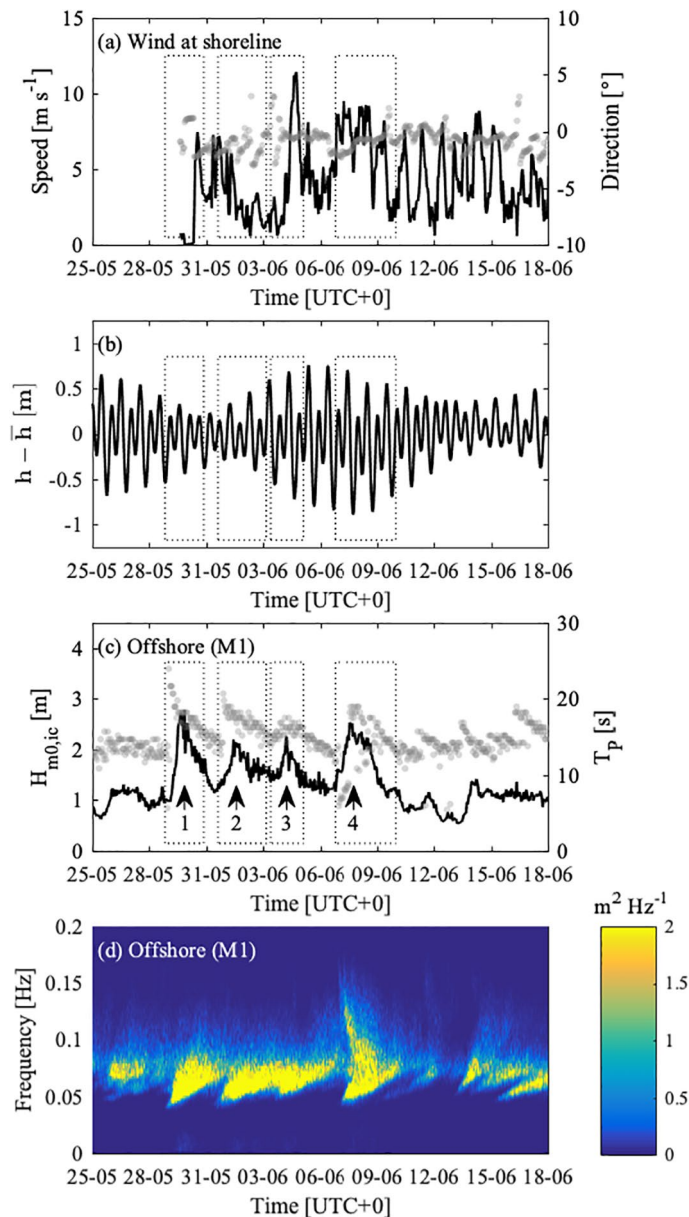


Figure 2. Incident forcing measured on the fore reef at M1 and at the shoreline. (a) The wind speed and direction measured at the shoreline. (b) The tidal variability measured at M1 in ~ 20 m water offshore of the reef crest. (c) The incident wave conditions measured at M1 with the incident wave height, $H_{m0,ic}$, shown in black and the peak wave period, T_p , associated with these waves is shown in gray. (d) A timelapse of the wave spectra which shows the offshore most of the energy is contained within the sea-swell frequency band. Four peaks in wave height are observed and indicated with arrows with the extent of the events indicated by the dotted boxes.

noticeably larger (up to 0.2 mm). These D values are consistent with the peak in D by mass collected in the sediment traps located at each site (Figure 4).

3.4. Suspended-Sediment Concentrations (SSC)

The SSC varied with the tide, as well as with the incident wave forcing (Figure 6). The OBS and ABS estimates of SSC measured 0.2 m above the bed (mab) were similar throughout the experiment (Figures 6b–6d). At each site, the average SSC decreased at low tide and increased with the higher tide. At T1 on the outer reef flat, early and late in the experiment (24–28 May and 9–20 June), the SSC was low ($1\text{--}6\text{ mg L}^{-1}$) and predominantly

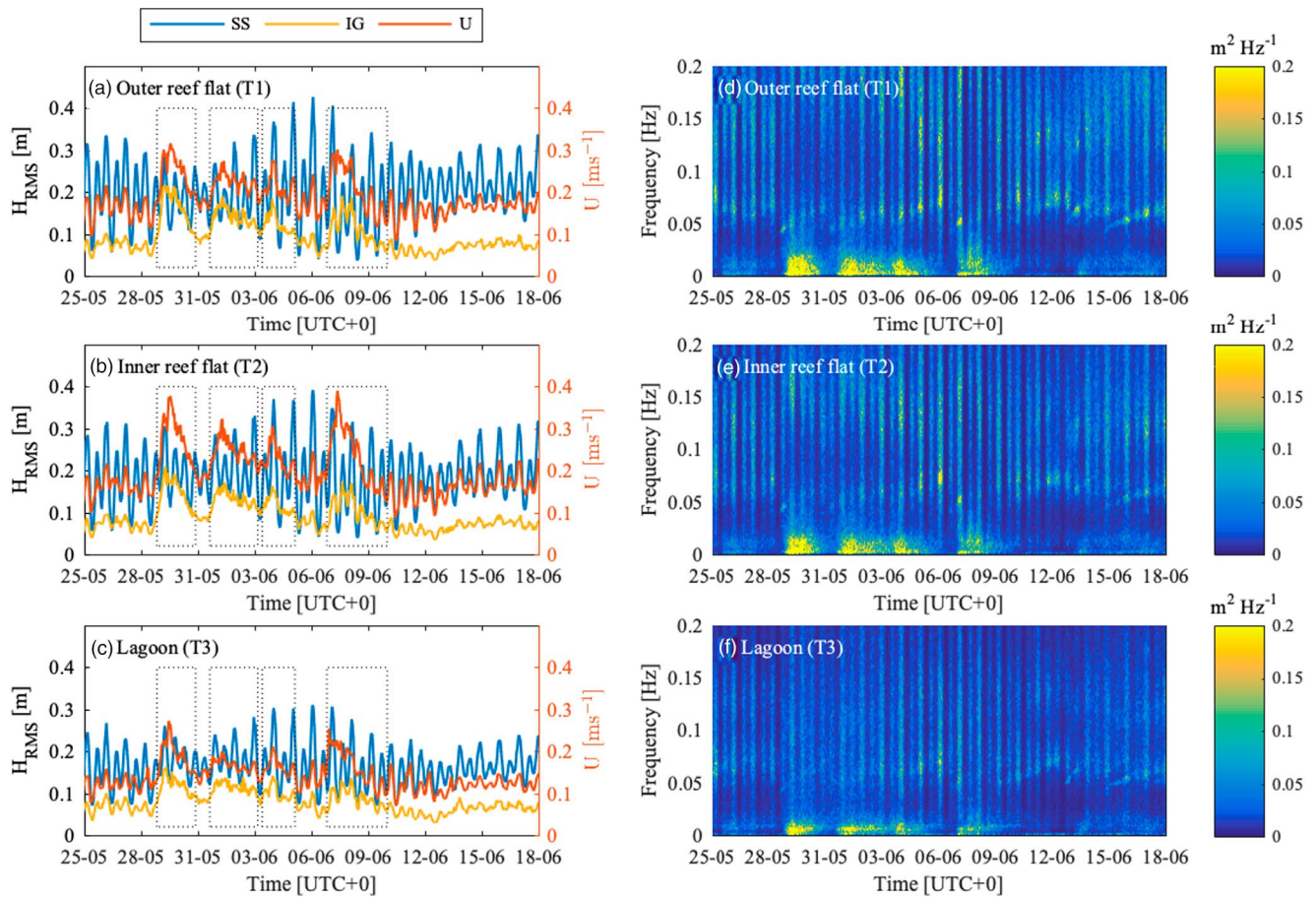


Figure 3. The waves and depth-averaged current measured at sites across the reef platform (T1–T3). Panels (a–c) show the hourly root mean squared wave height (H_{RMS}) for the sea-swell (SS) and infragravity (IG) frequency bands, along with the depth averaged mean current (U), while panels (d–f) show the wave energy spectra. (a, d) T1 on the outer reef flat. (b, e) T2 on the inner reef. (c, f) T3 in the lagoon. The four events, along with tidal variability, are clearly observed in the $H_{RMS,IG}$ and U across all reef sites whereas the $H_{RMS,SS}$ data varied only with the tide. Energy dissipation across the reef sites is clearly observed in both frequency bands as well as in the U .

exhibited tidal variability (Figure 6b). While the impact of the wave events on the SSC variability is apparent in the data at T1, only the first and fourth events resulted in a substantially greater SSC when compared to the typical outer reef flat variability. Whilst the $H_{m0,ic}$ were larger during the first event than during the fourth event (Figure 2c), the average SSC on the outer reef flat at T1 was slightly lower during the first event than during the fourth event (Figure 6b). This difference in SSC is due to the larger average high tide (i.e., near spring tide) that occurred during the fourth event, which enabled larger incident waves to propagate across the reef. In contrast, the first event occurred close to neap tide and the average high tide was lower. During the fourth event, the SSC on the reef flat was 2–3 times greater than the typical SSC observed at other times during the experiment. We note that the $H_{RMS,IG}$ and U in the first event were similar to the $H_{RMS,IG}$ and U in fourth event.

The SSC variability on the inner reef flat at T2 and in the lagoon at T3 was ~ 2 times greater than the SSC observed on the outer reef flat at T1 (Figures 6c and 6d). The SSC was slightly higher at T2 (1.5–15 mg L^{-1}) than at T3 (2–13 mg L^{-1}). At both sites, the change in magnitude of SSC with the semi-diurnal tide is apparent. Similar to T1, the first and fourth events are clearly visible in the data at T2, but the second or third events are less distinct. It is notable that during the first and fourth events, despite similar or slightly larger H_{RMS} at T2 than at T3, the peaks in SSC at T3 were larger than those measured at T2. This difference in the magnitude of the SSC peaks was clearly observed during the fourth event and also, to a lesser extent, during the first event. Furthermore, a reduction in the SSC variability was observed at T2 for a period of time after these events. In the case of the first event, this decrease in variability extended for a number of days (i.e.,

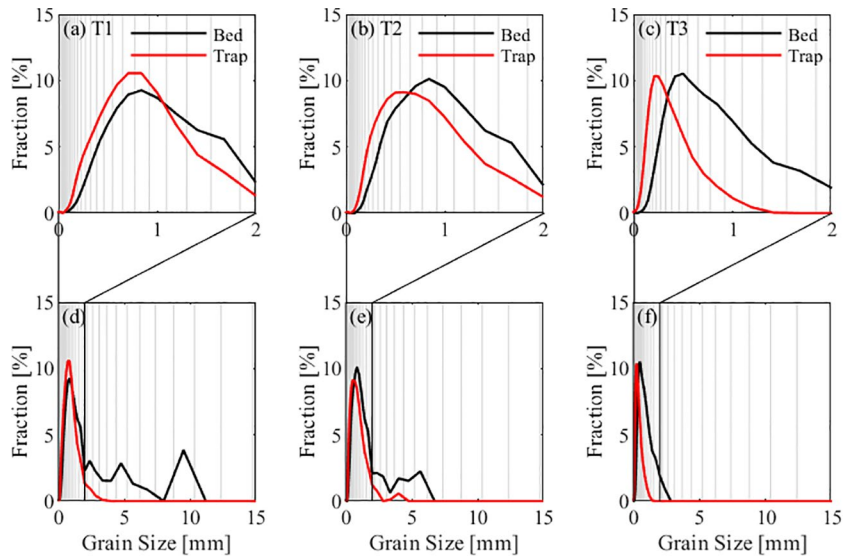


Figure 4. Seabed and suspended (trap) sediment grain size distributions. The peak in the grain-size distribution is shown in detail in top row, with the full distribution shown in the bottom row. (a, d) On the outer reef flat at T1. (b, e) On the inner reef flat at T2. (c, f) In the lagoon at T3. The gray lines show the resolution of the grain size distribution analysis. The grain size of the sediment collected in the suspended sediment trap is unimodal and thus suitable for the ABS and OBS calibration.

from 1 to 3 June). This is despite the SS and IG waves, as well as U , being similar or even greater magnitude than during nonevent periods (e.g., 14–18 June).

Profiles of the SSC indicate that at each site most of the sediment in suspension was located close to the seabed (Figures 6e–6g) below the elevations of the point measurements. On the outer reef flat at T1, the seabed level was constant during the experiment, with only small variations in the bed elevation measured (Figure 6e). Whilst there was a small increase in SSC throughout the water column at tidal timescales, the impact of the four events on the water column SSC is clearly observed. On the inner reef flat at T2, considerable bed variability occurred (Figure 6f). During the first event, the seabed elevation rapidly reduced and remained fairly flat for ~7 days. For a period of ~2 days prior to the fourth event, the elevation of the seabed increased before it again rapidly decreased during the fourth event. There was also a notable absence of peaks in SSC during these periods when compared to other times in the experiment, or at T3 in the lagoon where such rapid changes in bed elevation were not measured (Figure 6g).

3.5. Cumulative Suspended-Sediment Flux (SSF)

Despite the variability in hydrodynamic forcing (Figure 7a), the cumulative depth-integrated SSF contribution by SS (Q_{SS}) was consistently directed offshore on the inner reef flat at T2 and in the lagoon at T3, but

Table 3
Seabed and Suspended (Trap) Sediment Characteristics by Mass

Sample	Mud—<63 μ m (%)	Sand—63 μ m–2 mm (%)	Gravel—> 2 mm (%)	CaCO ₃ (%)	Terrigenous (%)	D_{50} (mm)
T1 Seabed	0.6	79.9	19.5	99.5	0.5	0.95
T1 Trap	1.3	95.9	2.8	99.5	0.5	0.67
T2 Seabed	0.6	87.2	12.2	99.5	0.5	0.86
T2 Trap	1.0	96.4	2.6	99.5	0.5	0.57
T3 Seabed	0.8	96.4	2.8	99.2	0.8	0.58
T3 Trap	5.3	94.7	0.0	98.3	1.4	0.24

Note. The calcium carbonate (CaCO₃) and terrigenous percentages are based on the sand fraction.

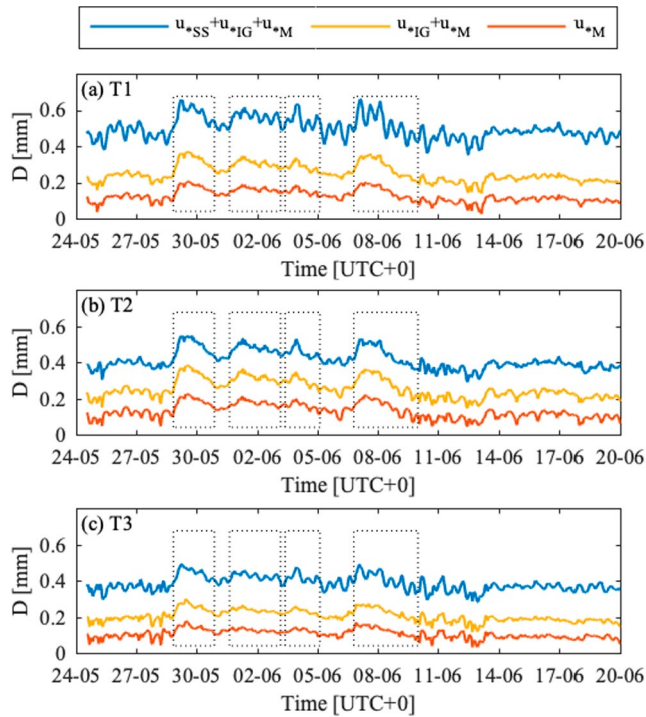


Figure 5. Grain size (D) predicted to be suspended from the bed due to shear stress (presented here as shear velocity) imposed on the bed by mean currents (u_M), u_M combined with infragravity waves (u_{IG}), and u_M combined with u_{IG} and sea-swell waves (u_{SS}). (a) On the outer reef at T1. (b) On the inner reef at T2. (c) In the lagoon at T3. The four events are indicated by the dotted boxes. Sea-swell waves are responsible for the suspension of the largest grain sizes and these predicted grain sizes agree with the peak by mass of the sediment trap grain size distribution at each site.

was similar on the outer reef flat at T1 and in the lagoon at T3 but slightly lower than at T2 ($0.5\text{--}3.5\text{ kg m}^{-1}\text{ h}^{-1}$). This similarity in flux was due to differences in the magnitude of U , which was consistently greater at T1 than at T3 (Figure 3), which offset differences in the SSC at each site. Thus, faster currents and lower concentration at T1 resulted in a similar flux of sediment as the lower currents and higher concentrations at T3. When U was small in comparison to the U observed during the four events, Q_M was also small. However, when the U increased even slightly above its fairly stable nonevent magnitude, Q_M rapidly increased. It is clear from these results that once sediment was suspended into the water column, Q_M made the dominant contribution to fluxes of suspended sediment across the reef.

3.6. SSC Wave Phase Variability

Whilst the decomposition of the contribution to the cumulative SSF demonstrated Q_M was the primary mechanism responsible for the transport of sediment in suspension, sediment was also transported offshore by SS waves and onshore by IG waves. Here, we consider how four different forcing conditions affect the vertical distribution of sediment throughout the wave cycle and how these forcing conditions affect the flux of sediment at each location across the study site.

When $H_{RMS,IG}$ was low and $H_{RMS,SS}$ was high ($\downarrow_{IG}\uparrow_{SS}$, Figure 8), the SSC on the inner reef flat at T2 and in the lagoon at T3 was much larger than the SSC on the outer reef flat at T1 (<0.5 vs. $2\text{--}3\text{ mg L}^{-1}$). At T2 and T3 where the SSC was large (Figures 8m–8o), the Q_{SS} was directed offshore at T2 but onshore at T3 due to differences in the phasing between waves and concentration at each of these sites (Figures 8d–8f). At T2, the SSC decomposed for SS frequencies (c_{SS}) increased near slack flow as the oscillatory velocity transitioned

was negligible at T1 on the outer reef flat (Figure 7b). Close inspection of Q_{SS} at T2 indicates that this transport exhibits a stepped (on-off) type pattern. Within a tidal cycle, the Q_{SS} increased from a near zero transport rate at approximately mid-falling tide, approached a maximum 1–2 h prior to low tide, before the rate reduced until it ceased at low tide and remained near zero as the tide increased (not shown). A similar transport pattern was also measured in the lagoon at T3. Most Q_{SS} occurred during nonevent periods at T2 at an average rate of $\sim 0.04\text{ kg m}^{-1}\text{ h}^{-1}$ (but could be as high as $0.07\text{ kg m}^{-1}\text{ h}^{-1}$). There were two periods of time when Q_{SS} was ~ 4 times smaller, 30 May to 4 June and 7–9 June. These periods were the same periods when the bed was flat (Figure 6b). In contrast, at T3 the Q_{SS} almost only occurred during the four events, although the transport rate was similar ($\sim 0.03\text{ kg m}^{-1}\text{ h}^{-1}$).

The cumulative depth-integrated SSF contribution by IG (Q_{IG}) over the duration of the experiment was approximately half of Q_{SS} (Figure 7c). The Q_{IG} was principally directed onshore on the outer reef flat at T1 and the inner reef flat at T2, but in the lagoon at T3 it alternated between being directed onshore and offshore. At T1, the Q_{IG} was directly related to the presence of the larger IG waves that occurred during each of the four events, with negligible Q_{IG} at other times during the experiment. During these events, the Q_{IG} ranged from 0.025 to $0.035\text{ kg m}^{-1}\text{ h}^{-1}$. The Q_{IG} was slightly smaller at T2 but was also directly related to the increase in $H_{RMS,IG}$. At T3, the Q_{IG} was almost always small ($<0.02\text{ kg m}^{-1}\text{ h}^{-1}$) and was briefly onshore directed during the first event but directed offshore at other times. Notably in contrast to Q_{SS} , the plateaus in Q_{IG} coincide with the reduction in $H_{RMS,IG}$ and not the state of the bed. Whilst the Q_{IG} was greatest during pulses of IG energy at T1 and T2, at T3 there was no clear relationship between Q_{IG} and the hydrodynamic forcing.

The cumulative depth-integrated SSF associated with the mean current (Q_M) was 2 orders of magnitude greater than the Q_{SS} and Q_{IG} (Figure 7d). The Q_M was greatest on the inner reef flat at T2, with a typical rate of $0.5\text{ kg m}^{-1}\text{ h}^{-1}$ and as high as $\sim 5\text{ kg m}^{-1}\text{ h}^{-1}$ during the events. The Q_M

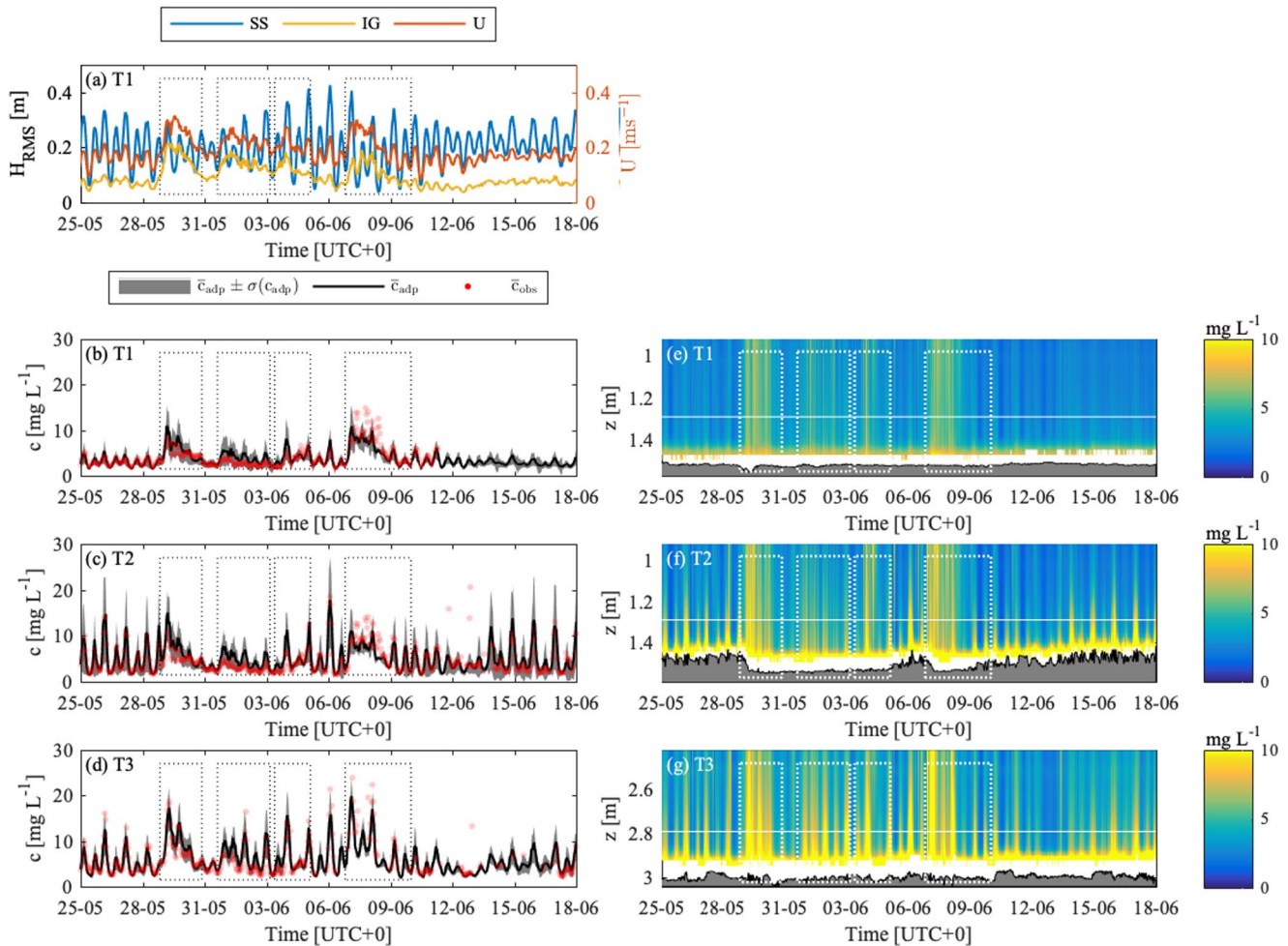


Figure 6. Wave and current forcing and the resulting suspended sediment concentrations. (a) The hourly sea-swell (SS) and infragravity (IG) root mean squared wave heights (H_{RMS}) and the depth-averaged mean current (U) on the outer reef flat at T1. The hourly suspended sediment concentrations (\bar{c}) measured by the acoustic Doppler profiler (ADP) and optical backscatter sensor (OBS) at each site. (b) On the outer reef at T1. (c) On the inner reef at T2. (d) In the lagoon at T3. The shaded areas indicate ± 1 standard (σ) deviation in the SSC time series data for each burst of ADP data. The vertical distribution of \bar{c} with the magnitude indicated by the colorbar in $mg L^{-1}$ at each site. (e) On the outer reef at T1. (f) On the inner reef at T2. (g) In the lagoon at T3. The average position of the seabed determined from the altimeters are indicated by the gray shaded areas. The horizontal white line indicates the position of the OBS and ABS data shown in the left column. The dotted boxes represent the four events. The highest \bar{c} was located close to the seabed below the elevation of typical point measurements.

from onshore to offshore-directed flow for each wave cycle and peaked just prior to the maximum offshore directed velocity. In contrast at T1 and T3, the c_{SS} was distributed across much of the wave cycle. While SSC decomposed for IG frequencies (c_{IG}) was larger than c_{SS} (Figures 8g–8i), the sediment was in suspension across almost the entire IG wave cycle, with only a slight bias during the offshore phase (Figures 8j–8l). Consequently, over a wave cycle the Q_{SS} was up to 4 times larger than the Q_{IG} (Figures 8p–8r). Thus, when the IG waves were small, the SSF associated with waves was dominated by SS processes.

When the $H_{RMS,SS}$ decreased to a value similar to $H_{RMS,IG}$ ($\downarrow_{IG} \downarrow_{SS}$, Figure 9), such as during the low tide non-event periods, the c_{SS} and c_{IG} was noticeably lower throughout the water column. Under these forcing conditions, the SSC was typically two thirds of the measured magnitude ($< 1 mg L^{-1}$) when $H_{RMS,SS}$ was larger (e.g., high tide), with little difference between the c_{SS} and c_{IG} (Figures 9m–9o). Whilst for these conditions there was little sediment suspension at any site, a slight elevation in the c_{SS} was typically measured when the oscillatory velocity transitioned from being directed onshore to offshore flow (Figures 9d–9f). A similar increase in c_{IG} was also measured but this increase occurred just after the peak onshore velocity. However, we note that these vertical phase-related distribution are normalized concentrations, and thus likely to

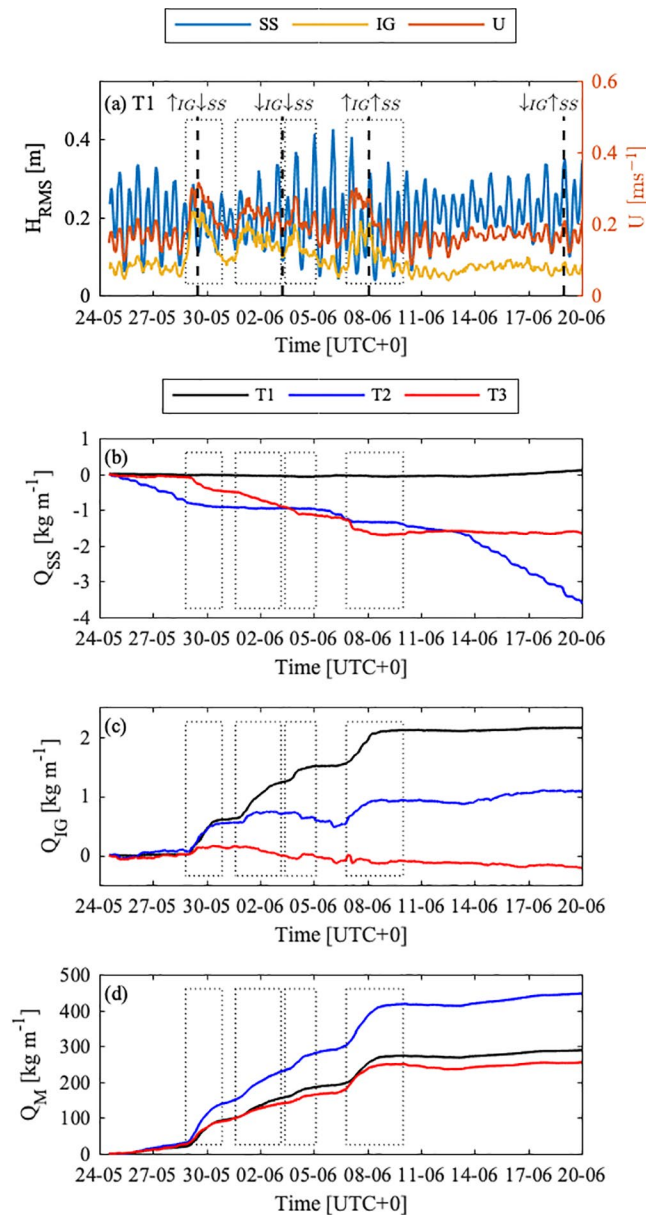


Figure 7. Wave and current forcing and the resulting mean and wave-driven cumulative depth-integrated suspended-sediment flux (Q) in $kg m^{-1}$. The hourly (a) sea-swell (SS) and infragravity (IG) root mean squared wave heights (H_{RMS}) and the depth-averaged mean current (U) on the outer reef flat at T1. The vertical dashed lines in (a) indicate cases considered in Section 3.6 and the extent of the four events are indicated by the dotted boxes. \downarrow_x indicates relatively “low” and \uparrow_x indicates relatively “high” SS or IG waves. (b) Sea-swell SSF (Q_{SS}) at the three sites. (c) Infragravity SSF (Q_{IG}) at the three sites. (d) Mean SSF (Q_M) at the three sites. Positive Q is directed onshore, and negative values are directed offshore. The Q_M was 2 orders of magnitude greater than Q_{SS} , which was directed offshore, and Q_{IG} , which was primarily directed onshore, but could also be directed offshore.

overemphasize the variability at these low concentrations (Figures 9g–9i). Due to the very low SSC and local velocities under these forcing conditions, there was little net SSF, except on the inner reef flat at T2 where the Q_{IG} was onshore but small (Figure 9q).

During each of the four events that occurred during the experiment, there was a noticeable increase in both $H_{RMS,SS}$ and $H_{RMS,IG}$ (Figure 3). During these events, IG waves were more asymmetric ($A_s = 0.45$ – 0.49) than for nonevent periods. When the $H_{RMS,IG}$ was relatively large and the $H_{RMS,SS}$ was small (but similar to $H_{RMS,IG}$, $\uparrow_{IG}\downarrow_{SS}$), the SSC throughout the water column was reduced and was predominantly located close to

the bed (Figure 10). These forcing conditions typically occurred during the four events but at low tide. For these conditions, the c_{SS} was similar to the low $H_{RMS,IG}$ and low $H_{RMS,SS}$ case ($<1 \text{ mg L}^{-1}$, Figures 10m–10o), whereas the c_{IG} was 2 times greater (Figures 10m–10o). The c was greatest during the onshore flow phase, which resulted in an onshore Q_{IG} (Figures 10g–10i). This flux was largest on the inner reef flat at T2 and ~ 3 times larger than the Q_{SS} . In contrast to the phase distribution of the c_{IG} , the c_{SS} was largest in magnitude during the transition from maximum onshore-to maximum offshore-directed oscillatory velocity (Figures 10d–10f). However, when combined with low SS velocities this resulted in negligible SSF at all sites.

If $H_{RMS,IG}$ remained relatively large and $H_{RMS,SS}$ increased, there was again an increase in SSC across the site ($\uparrow_{IG} \uparrow_{SS}$, Figure 11). This increase, however, resulted in a SSC that was similar to the low $H_{RMS,IG}$ and high $H_{RMS,SS}$ case, despite $H_{RMS,IG}$ being twice as large. At all sites, the Q_{SS} was directed offshore, with high c_{SS} measured during the oscillatory flow reversal that would persist through the offshore phase of the flow (Figures 11d–11f). This resulted in a net offshore Q_{SS} for all sites across the reef platform. In contrast, the c_{IG} was typically greatest during the onshore phase of the oscillatory flow cycle (Figures 11g–11i). Consequently, the Q_{IG} was directed onshore (Figures 11m–11o).

4. Discussion

4.1. Contribution of Suspended-Sediment Flux to Total Flux

Point measurements of SSC in reef environments are typically obtained ~ 0.15 – 0.2 mab (Larcombe et al., 1995, 2001; Ogston et al., 2004; Pomeroy et al., 2017; Presto et al., 2006; Storlazzi et al., 2004; Yahel et al., 2002). However, our profile measurements over 0.5 mab show that most of the elevated SSC occurs very near the bed (at <0.15 mab). Within this same near bed region the SSC is also highly variable. Thus, while point measurements that are typically obtained at 0.15–0.2 mab are suitable to understand concentration variability over different temporal and spatial scales, they are likely to underrepresent the actual magnitude of sediment transported in the water column. Over the duration of this experiment, 260–467 kg m^{-1} of sediment was transported in suspension, with the greatest transport on the inner reef flat at T2. Our estimates of SSF do not account for SSF >0.5 mab, which was beyond the range of our instrumentation, or very close to the seabed (≤ 0.075 mab) where we removed data to eliminate sidelobe effects. The exclusion of data higher in the water column is expected to be negligible, as the SSC and SSF tend toward zero higher in the water column (e.g., Figures 8m–8r). The exclusion of data close to the seabed is likely to result in an underestimate of the SSF close to the seabed where the SSC clearly exhibits an increasing trend.

These SSF rates were much lower than the bedload transport rates calculated at the same sites by Rosenberger et al. (2020). Rosenberger et al. (2020) found that on the inner reef flat bedload transport was supply limited, did not necessarily coincide with peak incident wave energy and was highly variable, even when the incident wave energy was consistent. At this location the bedload flux toward the shore ranged from 13 to 485 $\text{kg m}^{-1} \text{ d}^{-1}$, which over the duration of the experiment resulted in a transport rate of $\sim 1,565 \text{ kg m}^{-1}$. This represents 3–4 times greater flux by bedload than by suspended load. In the lagoon, Rosenberger et al. (2020) showed that the bedload transport would usually peak at the onset of events and then gradually slow. At this location the magnitude of bedload ranged from 20 to 231 $\text{kg m}^{-1} \text{ d}^{-1}$. Over the duration of the experiment this resulted in $\sim 485 \text{ kg m}^{-1}$ of sediment transported as bedload, which was 2 times greater than that transported in suspension. Bedload transport rates on the north and south side of the shoreline salient were 116 and 325 kg m^{-1} , respectively (Cuttler et al., 2019). For this reef system, and the observed forcing conditions, bedload is the dominant sediment transport mechanism. When the results of this study are combined with the bedload transport rates determined by Rosenberger et al. (2020), the average rate of total sediment flux from the reef at T2 toward the lagoon at T3 is 1.3 kg m^{-2} .

The reduction in SSC (Figures 7b and 7c) and SSF (Figures 6c and 6f) on the inner reef flat at T2 during and just after events coincided with the near flat-bed measurements (i.e., the absence of mobile sediment bed forms) observed by Rosenberger et al. (2020). There are a number of possible explanations for this reduction: (i) sediment was washed off the reef flat, leaving little sediment to be suspended (i.e., sediment was stripped leaving the underlying pavement exposed), (ii) the “wash out” of ripples due to sheet flow transport during events that reduces the efficiency of sediment resuspension (Nakato et al., 1977; O’Hara

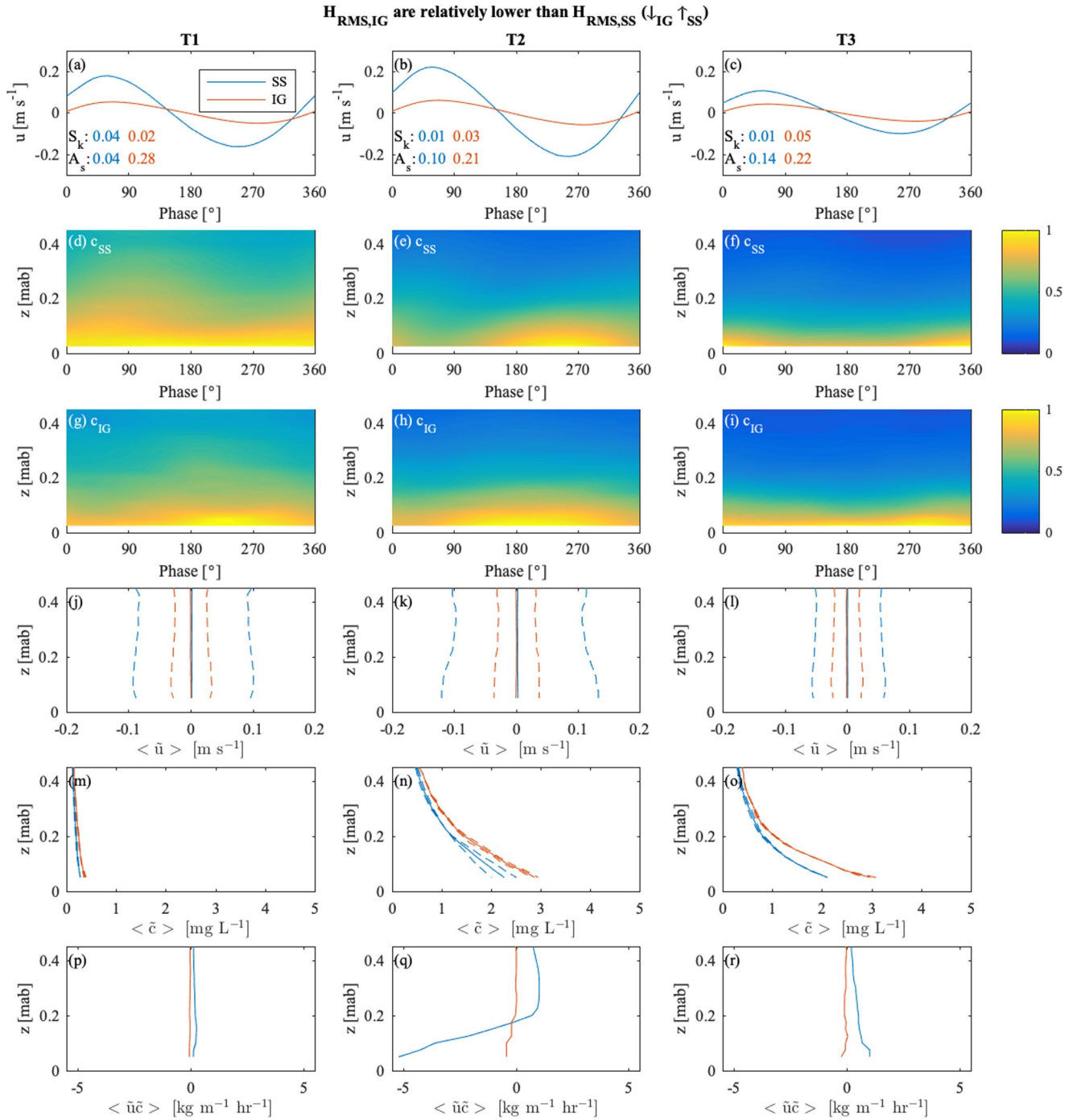


Figure 8. Coupling between waves, suspended sediment concentrations (c), and fluxes (SSF) at sea-swell (SS) and infragravity (IG) frequencies for the case where IG waves are relatively low compared to the SS waves ($\downarrow_{IG} \uparrow_{SS}$). The left column is for the outer reef flat at T1, middle column is on the inner reef flat at T2, and the right column is in the lagoon at T3. (a–c) The ensemble averaged wave velocity at ~ 0.15 mab for SS and IG frequencies with the skewness (S_k) and asymmetry (A_s) for the SS (blue) and IG (red) waves noted in the bottom left of each panel. (d–f) The ensemble average of c at each phase for SS frequencies distributed over ~ 0.5 mab. (g–i) The ensemble average of c at each phase for IG frequencies distributed over ~ 0.5 mab. The color bars indicate the phase averaged and normalized c . (j–l) The average of all onshore velocity profiles and the average of all offshore velocity profiles (dashed lines), as well as the wave-averaged profile (solid lines) for SS and IG frequencies. (m–o) The average of all onshore SSC profiles and the average of all offshore SSC profiles (dashed lines), as well as the wave-averaged profile (solid lines) for SS and IG frequencies. (p–r) The wave-averaged SSF at SS and IG wave frequencies. The largest SSF occurred at T2 and was directed offshore at SS frequencies.

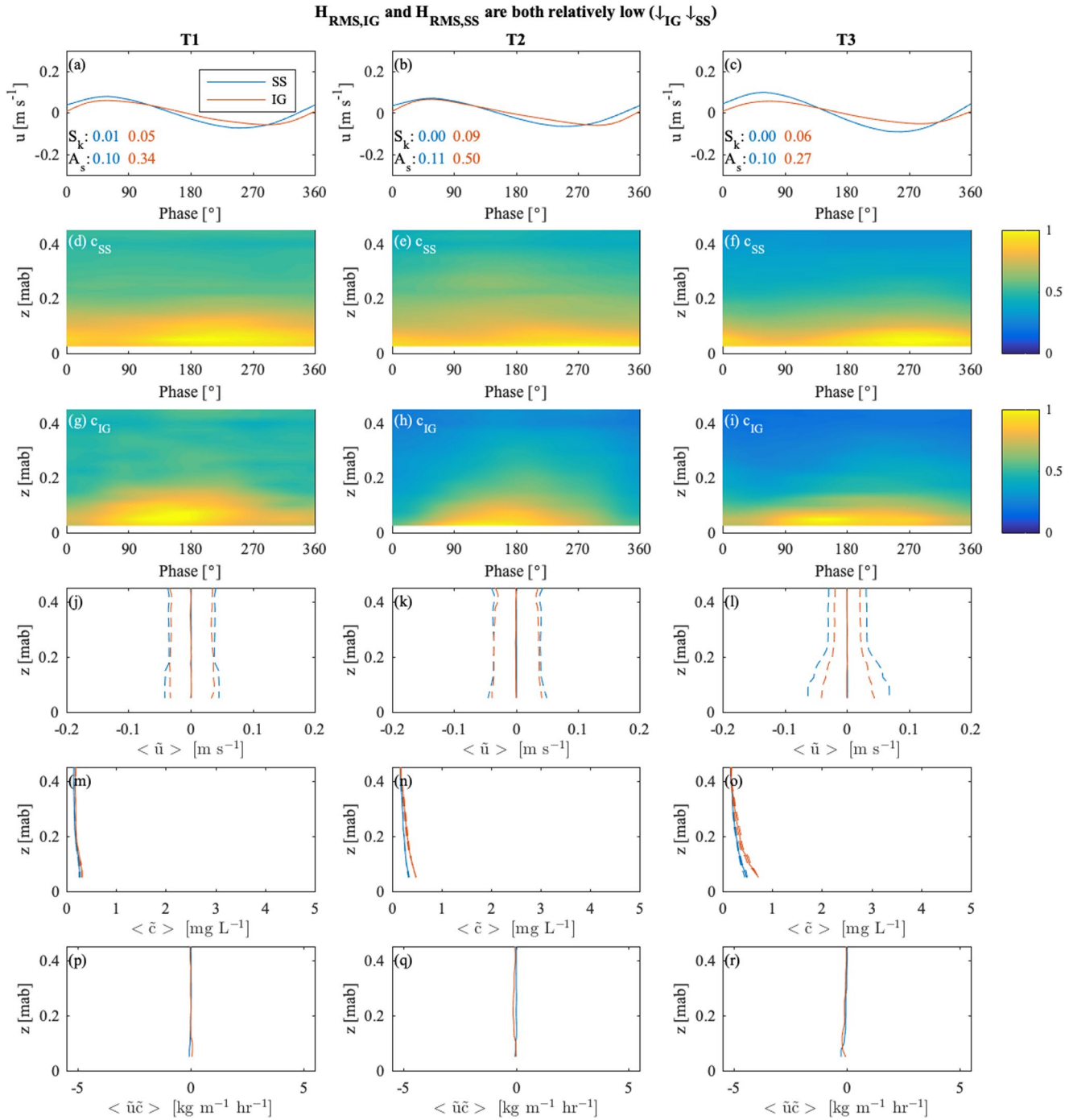
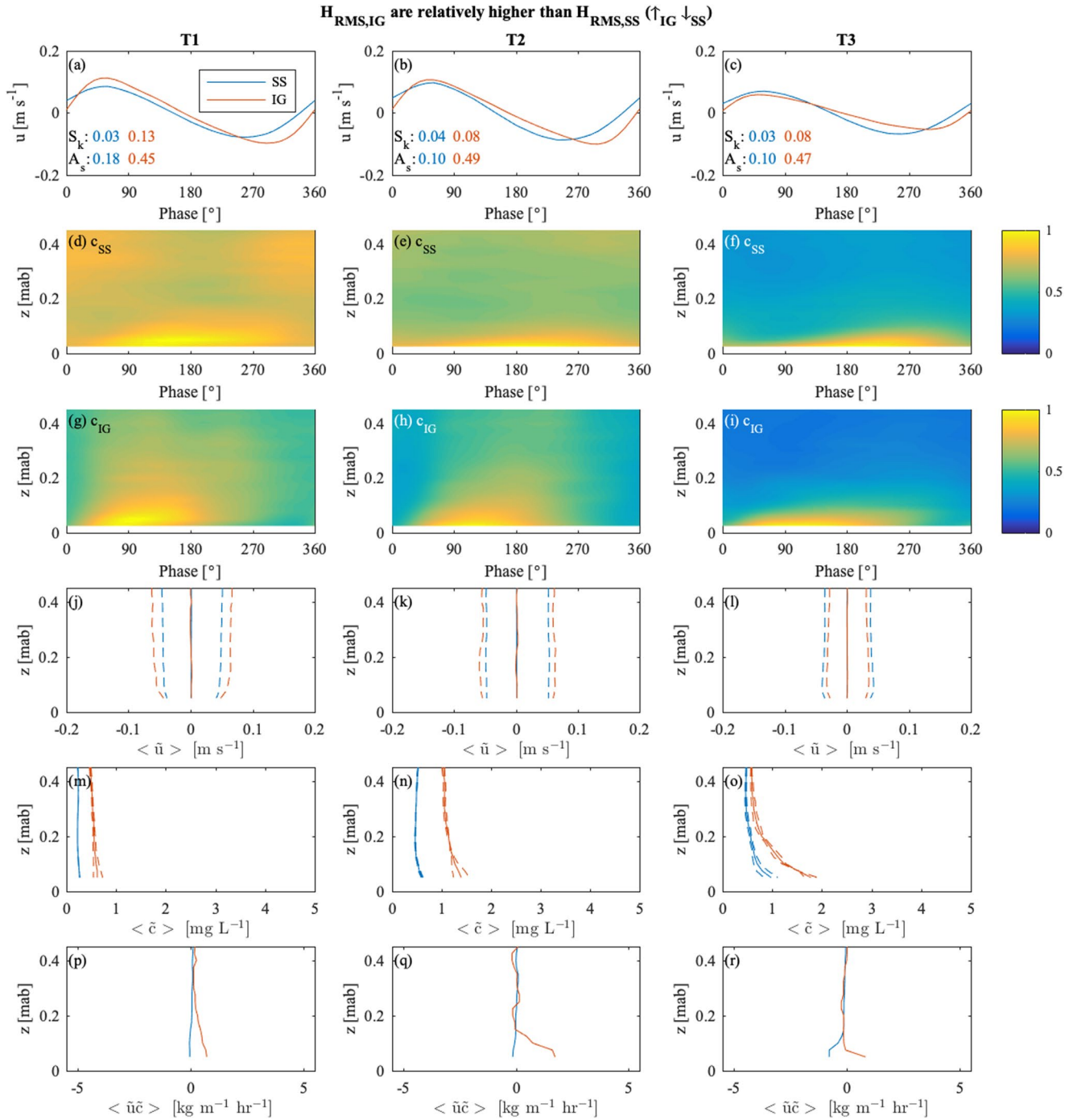


Figure 9. Coupling between waves, suspended sediment concentrations (c), and fluxes (SSF) at sea-swell (SS) and infragravity (IG) frequencies for the case where IG waves and SS are both relatively low ($\downarrow_{IG} \downarrow_{SS}$). The left column is for the outer reef flat at T1, middle column is on the inner reef flat at T2, and the right column is in the lagoon at T3. (a–c) The ensemble averaged wave velocity at ~ 0.15 mab for SS and IG frequencies with the skewness (S_k) and asymmetry (A_s) for the SS (blue) and IG (red) waves noted in the bottom left of each panel. (d–f) The ensemble average of c at each phase for SS frequencies distributed over ~ 0.5 mab. (g–i) The ensemble average of c at each phase for IG frequencies distributed over ~ 0.5 mab. The color bars indicate the phase averaged and normalized c . (j–l) The average of all onshore velocity profiles and the average of all offshore velocity profiles (dashed lines), as well as the wave-averaged profile (solid lines) for SS and IG frequencies. (m–o) The average of all onshore SSC profiles and the average of all offshore SSC profiles (dashed lines), as well as the wave-averaged profile (solid lines) for SS and IG frequencies. (p–r) The wave-averaged SSF at SS and IG wave frequencies. When $H_{RMS,SS}$ and $H_{RMS,IG}$ are similar but small, little sediment is suspended and the flux is negligible.



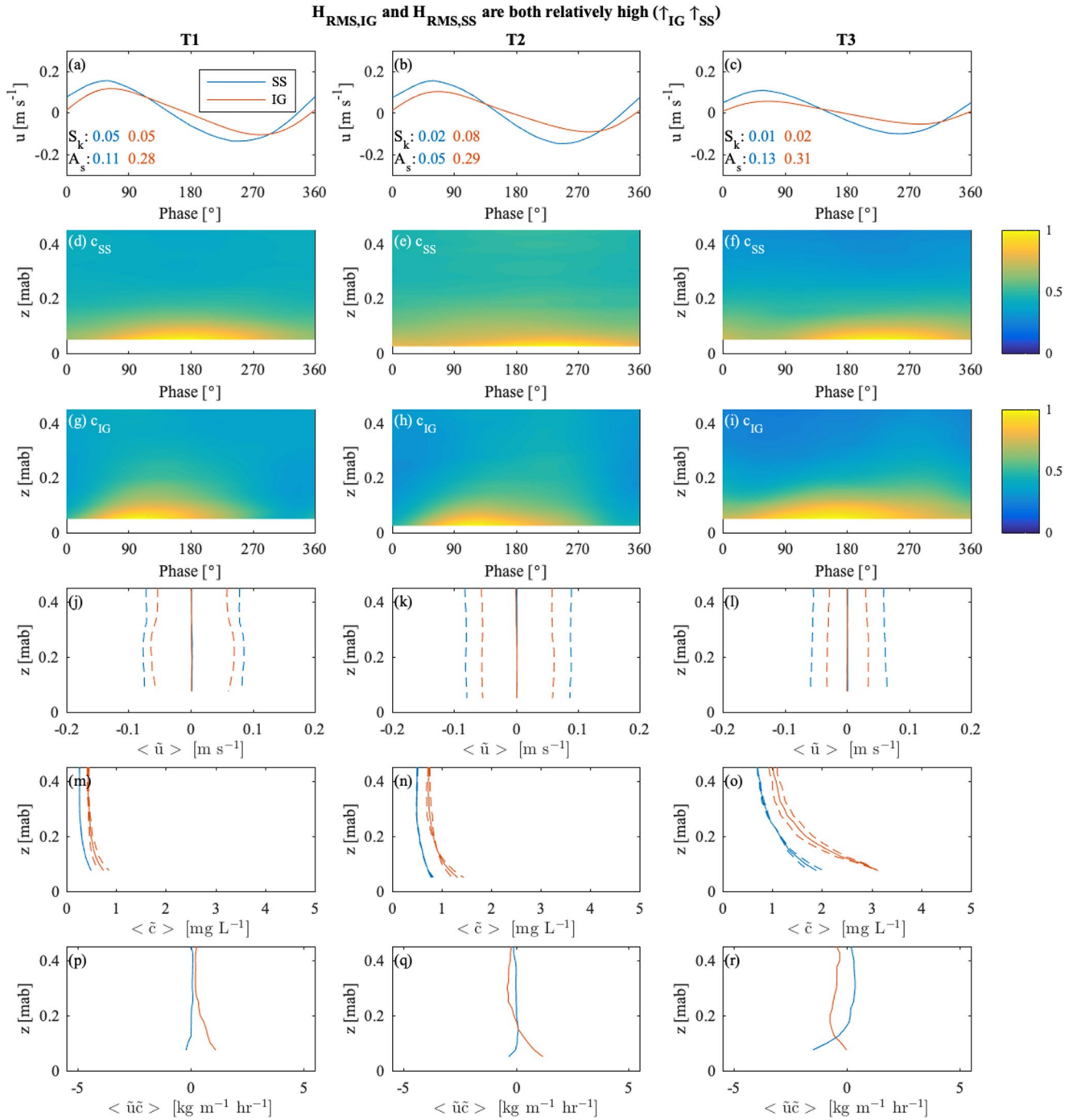


Figure 11. Coupling between waves, suspended sediment concentrations (c), and fluxes (SSF) at sea-swell (SS) and infragravity (IG) frequencies for the case where $H_{RMS,IG}$ and $H_{RMS,SS}$ are both relatively high ($\uparrow_{IG} \uparrow_{SS}$). The left column is for the outer reef flat at T1, middle column is on the inner reef flat at T2, and the right column is in the lagoon at T3. (a–c) The ensemble averaged wave velocity at ~ 0.15 mab for SS and IG frequencies with the skewness (S_k) and asymmetry (A_s) for the SS (blue) and IG (red) waves noted in the bottom left of each panel. (d–f) The ensemble average of c at each phase for SS frequencies distributed over ~ 0.5 mab. (g–i) The ensemble average of c at each phase for IG frequencies distributed over ~ 0.5 mab. The color bars indicate the phase averaged and normalized c . (j–l) The average of all onshore velocity profiles and the average of all offshore velocity profiles (dashed lines), as well as the wave-averaged profile (solid lines) for SS and IG frequencies. (m–o) The average of all onshore SSC profiles and the average of all offshore SSC profiles (dashed lines), as well as the wave-averaged profile (solid lines) for SS and IG frequencies. (p–r) The wave-averaged SSF at SS and IG wave frequencies. The SSF at SS frequencies was directed offshore across the study area, but the SSF at IG frequencies was directed onshore on the reef flat but directed offshore in the lagoon.

Murray et al., 2011; Sleath & Wallbridge, 2002), or (iii) the composition of the bed sediment changed. It is difficult to determine the precise cause of this reduction in the sediment based on the data in this study alone; however, Rosenberger et al. (2020) argued based on a detailed analysis of the bedload dynamics that bed sediment limitation was likely to be a key factor. Our results demonstrate that once the bed is flat, there was little SSF and SSC was reduced. This is despite the u_{*SS} (Figure 4) being sufficiently large to continue to suspend the typical sediment grain size D observed in the sediment trap (Figure 3). We note that the SSF due to IG waves continued to transport sediment during these times. This suggests that the length scales of SSF for the SS waves are small relative to the IG waves; SSF by SS may be locally generated whereas SSF by IG may be advected across the site. Importantly, both bedload and suspended load is clearly affected by sediment availability in this reef environment. The mechanism that transports sediment onto the reef once the reef has been stripped of sediment remains unclear but may be wave transport (discussed later) or the transport of offshore sediment up onto the reef under certain incident conditions (Storlazzi et al., 2004).

Finally, how the SSF varies both along the direction of transport and alongshore due to variability in sediment availability and the fine scale composition of the bed remains poorly quantified in this study. Conventional sediment transport predictions as well as the approach taken in this study assume the bed is fully occupied by sediment of unlimited supply, which is clearly not the case on many coral reefs. In reality, the sediment is interspersed between roughness elements that may occupy a large proportion of the planform area of a reef, thereby reducing the area over which the sediment can be entrained. Thus, sediment may be transported through regions where sediment is exposed but in other regions where the roughness occupies a large proportion of the bed, little sediment may be transported. Thus, irrespective of the sediment grain size distribution, there can be limited sediment available for suspension on the reef flat. Whilst not the focus of this study and the data are insufficient to spatially resolve the differences in sediment flux, it would be reasonable to assume that more sediment would be transported around and through roughness elements than over areas of the bed where the roughness occupies a large proportion of the bed.

4.2. Suspended-Sediment Fluxes by Waves and Mean Currents

In this study, the transport of sediment in suspension due to the phase-differences between the wave velocities and the SSC (Equation 3) was typically only 1% of the sediment transported by mean currents. The comparatively high transport rates due to mean currents was due to the strong cross-reef currents that develop from the setup generated by the radiation-stress gradients induced by wave breaking on the fore reef (Becker et al., 2014; Longuet-Higgins & Stewart, 1964). The presence of the lagoon and breaks in the reef at this site enable the water setup on the reef flat to circulate through the reef system and exit via the channels (Pomeroy et al., 2018). Whilst there was some tidal variability in the magnitude of this mean current, the vertical distribution of SSC was strongly affected by the magnitude of the $H_{RMS,SS}$ (Figure 7). Greater SSC was observed when $H_{RMS,SS}$ was larger. Our estimates of u_* and D show that the D that could be suspended by mean currents (Figure 5) was consistently smaller than the D observed in the trap sediment samples (Figure 4). This is consistent with other studies that have quantified the magnitude of bed u_* attributed to waves and currents in reef environments, which have shown that SS waves are often required to suspend much of the sediment observed both on the bed as well as in suspension (e.g., Pomeroy et al., 2018; Presto et al., 2006).

Notably, not all reef systems have strong cross-reef currents. For example, relatively alongshore uniform reefs (Storlazzi & Jaffe, 2008) or shallow shore-attached fringing reefs without a lagoon (Ogston et al., 2004; Péquignet et al., 2014; Presto et al., 2006) are systems where the relative importance of sediment transport by waves could be expected to be of greater relative importance than the transport by mean currents. The importance of wave-driven transport was also demonstrated in the 1-D laboratory study by Pomeroy et al. (2015), which showed that for a fringing reef system with a shallow reef flat the transport of sediment by waves could be similar and in some cases greater than bedload transport.

4.3. Sea-Swell and Infragravity Wave-Driven Suspended-Sediment Flux

The state of the seabed and the shape of the waves at a given location affect the magnitude and direction of sediment transport. In this study, there were noticeable differences between when SSC was greatest within the SS and IG wave phase cycle. The c_{SS} started to increase in magnitude as the flow approached peak on-

shore velocity and was typically at a maximum just after flow reversal. The c_{SS} then decreased during the offshore flow phase. Previous studies have shown that this pattern of suspension over a wave cycle is due to the vortex shedding off bed formations such as ripples that occurs as the vortex is advected over the ripple crest around the instant of SS flow reversal (Nakato, 1977; Sleath & Wallbridge, 2002; O' Hara Murray et al., 2011). This vortex-induced suspension also entrains sediment to considerably greater heights for a given hydrodynamic condition than would be suspended from a flat bed that relies on turbulent diffusion to lift sediment into the water column (Thorn, 2002; Bijker, 1967; Nakato, 1977; Davies & Thorne, 2005; Van der Werf, 2007; Nielsen, 1992; Thorne et al., 2009). Rosenberger et al. (2020) showed that ripples are present on the bed at both the inner reef flat at T2 and in the lagoon at T3, but were not observed on the outer reef flat at T1. Despite the absence of organized ripples on the reef flat, the phase observations in this study suggests that vortices develop and suspend sediment from the bed, perhaps due to reef flat bed variability (e.g., roughness). Wave nonlinearities such as asymmetric and skewed wave forms (Cheriton et al., 2020) may also contribute to the flux of sediment, particularly closer to the reef crest (Bramante et al., 2020).

In contrast, the c_{IG} typically increased just prior to the peak onshore velocity and was at a maximum just after this peak velocity. This pattern of suspension is consistent with the suspension of sediment due to stresses imposed on the bed (e.g., Davies & Thorne, 2008). When the waves are skewed (sharp high crests and broad shallow troughs) high crest velocities are generated in the onshore direction (Hsu & Hanes, 2004; Marino-Tapia et al., 2007). If these waves are also asymmetric (forward pitched saw tooth-type waves) strong fluid acceleration at the front face of these waves further enhance the mobilization and transport of sediment (Drake & Calantoni, 2001; Terrile et al., 2006). Whilst the phasing observed in this experiment suggests that sediment is suspended from the bed by IG waves, the u_{*IG} was small and thus these waves could only suspend fine sediment even under these nonlinear wave conditions. (Figure 5). An alternative explanation could be the relationship between SS and IG waves as they propagate across the reef and lagoon. On a moderately sloping beach where $H_{IG}/H_{SS} < 0.4$, de Bakker et al. (2016) demonstrated that the sediment flux is related to the correlation of the infragravity-wave orbital motion with the sea-swell wave envelope. That study showed that when large SS waves are present during negative IG velocities (bound infragravity wave case, negative correlation), Q_{IG} is directed offshore. However, when the correlation is positive (free IG waves), the largest SS waves are present during positive infragravity velocities and Q_{IG} is directed onshore. This latter case more closely relates to the dynamics observed in reef environments where it has been shown that IG waves generated on the reef flat typically propagate across the reef and lagoon as free waves (Pomeroy, Lowe, et al., 2012; Van Dongeren et al., 2013). For the two phase-averaged cases where $H_{IG}/H_{SS} < 0.4$, we observed that for the low $H_{RMS,IG}$ and high $H_{RMS,SS}$ case the SSF was directed slightly offshore. We note that very little sediment was in suspension; however, it is possible that this mechanism may reinforce the offshore-directed SSF by SS waves and contribute to the return of sediment to the inner reef.

de Bakker et al. (2016) also noted that when the infragravity waves are relatively large ($H_{IG}/H_{SS} > 0.4$), most sediment is suspended during negative infragravity velocities, and Q_{IG} is offshore directed. There were three short periods during this experiment where these conditions occurred and the SSF due to IG waves was indeed offshore directed. However, at all other times and also for the two phase-averaged cases where $H_{IG}/H_{SS} > 0.4$, the SSF was onshore directed. Further research is required to explore if and how the model by de Bakker et al. (2016) needs to be modified for application to coral reefs. Nevertheless, our results suggest that when IG waves are present, and under certain conditions, they can be an efficient sediment transport mechanism but that most of this sediment flux is onshore directed. This is consistent with the laboratory experiments by Pomeroy et al. (2015) that suggested that sediment transported at IG frequencies could be equal or greater than that transported at SS frequencies when $H_{RMS,IG}$ was similar or larger than $H_{RMS,SS}$.

4.4. Influence on Reef Sediment Distributions

Many reef studies have shown that sediment is continually transported from the reef to the shoreline and that bed sediment becomes progressively finer closer to the shoreline (e.g., Calhoun & Field, 2008). This change in bed sediment size is usually attributed to the overall breakdown of sediment from the reef to the shoreline along with the dissipation of waves and currents over the reef and lagoon. The lower wave and current energy allows finer sediment to settle out of the water column and be deposited on the seabed. However, this study demonstrates that the magnitude and direction of the SSF is not only dependent on the

mean current and wave energy but is also affected by phase coupling between IG and SS waves with SSC resuspension from the seabed.

Our results indicate that in the absence of IG waves, a mixture of sediment grain sizes is suspended into the water column during the SS oscillatory flow reversal. For this suspension mechanism, coarser sediment fractions can be expected to settle out of suspension during the ensuing offshore wave phase while finer sediment fractions persist in suspension to be deposited on the bed during the subsequent onshore wave phase. The cumulative impact of these waves is to partition finer sediment toward the shoreline and coarser sediment toward the reef flat. Our results suggest that offshore-directed transport of sediment may be greatest during nonevent periods and thus this may be a mechanism that contributes to the return of sediment to the reef flat once it has been washed off into the lagoon during larger events. When IG wave energy is high, such as during the events, the coupling between SS and IG waves results in higher SSC during the peak onshore IG wave phase. During this peak, SS waves were larger due to the increase in the water depth facilitated by the IG waves and sediment suspended by these waves can be transported considerable distances. For coarser sediment, this sediment may be transported shoreward close to the seabed while finer sediment that is suspended higher in the water column may be transported toward the reef flat (i.e., the opposite case to the SS wave only case). When combined with the tendency for mean currents to transport large quantities of sediment, our results suggest that waves may be particularly important to the sorting of coarser sediment that could not otherwise be transported in suspension.

4.5. Implications for Future Changes to Sediment Transport Mechanisms

The quantification of sediment transport throughout a reef system is critical to predict a range of impacts including the evolution of the adjacent shoreline. Our study examined this concentration distribution in detail and the fairly unimodal suspended-sediment distribution (Figure 4) enabled us to use acoustic backscatter to resolve these concentrations. An implicit assumption in our analysis is that this distribution remains fairly representative throughout the experiment, which is likely to be the case for the relatively moderate forcing conditions observed in this experiment. Further research is required to quantify the extent to which this sediment distribution changes due to different forcing and consequently what this may mean for suspended-sediment transport. However, we note that observations by Cuttler et al. (2018) suggest when this same reef was subjected to cyclone forcing, most of the wave growth across the site was due to wind; the incident waves continued to be depth-limited and efficiently dissipated on the fore reef. Thus, for noncyclonic but still energetic forcing, this forcing may not substantially impact the sediment distribution due to depth limitations imposed by the reef on the wave height.

It is clear from this study that most suspended sediment transport occurs during episodic events. The presence of SS and IG waves during these events results in substantial cross-reef transport of suspended sediment by mean currents (Figure 7). As sea levels increase, it may be expected that more sediment may initially be transported as larger waves propagate onto reefs and wave generated cross-reef currents remain similar or even larger than at present. This case could be expected to persist until such time that the increase in sea level is a substantial proportion of the tidal range. As sea levels continue to rise, cross-reef currents could then be expected to decrease in magnitude due to reduced wave breaking on the fore reef, which would reduce the water level setup on the reef that drives cross-reef currents (e.g., Becker et al., 2014; Vetter et al., 2010). Under these conditions, the relative importance of sediment transported in suspension by SS and IG waves is likely to increase. It remains unclear from the results of this study how these changes will affect the net cross-reef transport of sediment in suspension. Bramante et al. (2020) recently showed, using the nonhydrostatic numerical model XBeach, that for increased sea level the wave height, skewness, and shear stress imposed on the bed are likely to increase cross-reef sediment transport. However, that study also showed that changes to the incident waves on the fore reef would also reduce the sediment transported onto the reef flat from the fore reef. Our results show that the sediment transport on the reef flat may already be supply limited. Given there is a substantial flux of sediment from the reef into the lagoon, any reduction in supply can therefore be expected to have substantial impacts for sediment redistribution throughout a reef-lagoon system as well as to the adjacent shoreline.

5. Conclusions

In this study, we investigated the processes that drive the cross-reef transport and vertical distribution of suspended sediment across a reef platform, as well as how these distributions varied due to differences in the relative magnitude of sea-swell waves, infragravity waves, and mean currents. The main results of this study are as follows:

1. The morphology of a reef substantially attenuates waves in reef-lagoon systems. Consequently, most suspended sediment is transported close to the bed due to the low wave conditions. When sediment is suspended higher into the water column by sea-swell waves, this occurs during the oscillatory flow transition and often when ripples are present on the seabed. At infragravity frequencies this resuspension occurs during the onshore velocity phase.
2. For reef-lagoon systems where cross-reef currents can develop, SSF by mean currents is substantially greater (in this study by 2 orders of magnitude) than the flux by waves. However, waves still transport of sediment offshore at sea-swell frequencies and onshore at infragravity frequencies.
3. When compared to the transport of sediment by bedload, this study shows that bedload is 3–4 times greater than the depth-integrated SSF.

Data Availability Statement

Data sets analyzed in this manuscript are available from the USGS ScienceBase at <https://doi.org/10.5066/P9PEIA2S>. Any use of trade, firm, or product names is for descriptive purposes only and does not imply endorsement by the U.S. Government.

Acknowledgments

This project was funded by the U.S. Geological Survey Coastal and Marine Hazards and Resources Program, The University of Western Australia, and The Australian Research Council via the ARC Centre of Excellence for Coral Reef Studies. The authors would like to thank Carlin Bowyer, Anton Kuret, and Michael Cuttler (UWA) and Josh Logan (USGS) for their support in the field. The authors would like to thank Jessica Lacy (USGS) for her peer review of an earlier version of this manuscript and her helpful discussions, as well as the anonymous reviewers for their considered feedback that made a valuable contribution to this study. A. W. Pomeroy is grateful for the support of the Australian-America Fulbright Commission, who supported part of this research.

References

- Barber, S. (2002). *Laboratory procedures and grain size analysis of terrigenous and carbonaceous sediment of the fringing reef of Molokai, Hawaii*. San Francisco State University Thesis.
- Becker, J. M., Merrifield, M. A., & Ford, M. (2014). Water level effects on breaking wave setup for Pacific Island fringing reefs. *Journal of Geophysical Research: Oceans*, *119*(2), 914–932. <https://doi.org/10.1002/2013JC009373>
- Bijker, E. W. (1967). *Some considerations about scales for coastal models with movable bed*. Retrieved from <http://repository.tudelft.nl/view/ir/uuid:cdf2f061-3fe6-4361-a0e7-636fc69c9eca/>
- Bramante, J. F., Ashton, A. D., Storlazzi, C. D., Cheriton, O. M., & Donnelly, J. P. (2020). Sea level rise will drive divergent sediment transport patterns on fore reefs and reef flats, potentially causing erosion on Atoll Islands. *Journal of Geophysical Research: Earth Surface*, *125*(10), e2019JF005446. <https://doi.org/10.1029/2019JF005446>
- Brander, R. W., Kench, P. S., & Hart, D. (2004). Spatial and temporal variations in wave characteristics across a reef platform, Warraber Island, Torres Strait, Australia. *Marine Geology*, *207*(1–4), 169–184. <https://doi.org/10.1016/j.margeo.2004.03.014>
- Buckley, M. L., Lowe, R. J., Hansen, J. E., & Van Dongeren, A. R. (2015). Dynamics of wave setup over a steeply sloping fringing reef. *Journal of Physical Oceanography*, *45*(12), 3005–3023. <https://doi.org/10.1175/JPO-D-15-0067.1>
- Buckley, M. L., Lowe, R. J., Hansen, J. E., & Van Dongeren, A. R. (2016). Wave setup over a fringing reef with large bottom roughness. *Journal of Physical Oceanography*, *46*, 2317–2333. <https://doi.org/10.1175/JPO-D-15-0148.1>
- Calhoun, R. S., & Field, M. E. (2008). Sand composition and transport history on a fringing coral reef, Molokai, Hawaii. *Journal of Coastal Research*, *24*(5), 1151–1160. <https://doi.org/10.2112/06-0699.1>
- Cheriton, O. M., Storlazzi, C. D., & Rosenberger, K. J. (2016). Observations of wave transformation over a fringing coral reef and the importance of low-frequency waves and offshore water levels to runup, overwash, and coastal flooding. *Journal of Geophysical Research: Oceans*, *121*(5), 3121–3140. <https://doi.org/10.1002/2015JC011231>
- Cheriton, O. M., Storlazzi, C. D., & Rosenberger, K. J. (2020). In situ observations of wave transformation and infragravity bore development across reef flats of varying geomorphology. *Frontiers in Marine Science*, *7*, 16. <https://doi.org/10.3389/fmars.2020.00351>
- Coronado, C., Candela, J., Iglesias-Prieto, R., Sheinbaum, J., López, M., & Ocampo-Torres, F. J. (2007). On the circulation in the Puerto Morelos fringing reef lagoon. *Coral Reefs*, *26*, 149–163. <https://doi.org/10.1007/s00338-006-0175-9>
- Cuttler, M. V. W., Hansen, J. E., Lowe, R. J., & Drost, E. J. F. (2018). Response of a fringing reef coastline to the direct impact of a tropical cyclone. *Limnology and Oceanography Letters*, *3*(2), 31–38. <https://doi.org/10.1002/lol2.10067>
- Cuttler, M. V. W., Hansen, J. E., Lowe, R. J., Trotter, J. A., & McCulloch, M. T. (2019). Source and supply of sediment to a shoreline salient in a fringing reef environment. *Earth Surface Processes and Landforms*, *44*(2), 552–564. <https://doi.org/10.1002/esp.4516>
- Cuttler, M. V. W., Lowe, R., Hansen, J., Falter, J., & Pomeroy, A. W. M. (2015). *Grainsize, composition and biform patterns in a fringing reef system*. In The Proceedings of Coastal Sediments. https://doi.org/10.1142/9789814689977_0239
- Davies, A. G., & Thorne, P. D. (2005). Modeling and measurement of sediment transport by waves in the vortex ripple regime. *Journal of Geophysical Research: Oceans*, *110*, C05017. <https://doi.org/10.1029/2004JC002468>
- Davies, A. G., & Thorne, P. D. (2008). Advances in the study of moving sediments and evolving seabeds. *Surveys in Geophysics*, *29*(1), 1–36. <https://doi.org/10.1007/s10712-008-9039-x>
- de Bakker, A. T. M., Brinkkemper, J. A., van der Steen, F., Tissier, M. F. S., & Ruessink, B. G. (2016). Cross-shore sand transport by infragravity waves as a function of beach steepness. *Journal of Geophysical Research: Earth Surface*, *121*, 1786–1799. <https://doi.org/10.1002/2016JF003878>

- Demirbilek, Z., Nwogu, O. G., & Ward, D. L. (2007). *Laboratory study of wind effect on runup over fringing reefs. Report 1: Data Report*. Coastal and Hydraulics Laboratory: US Army Corps of Engineers.
- Drake, T. G., & Calantoni, J. (2001). Discrete particle model for sheet flow sediment transport in the nearshore. *Journal of Geophysical Research*, 106(C9), 19859–19868. <https://doi.org/10.1029/2000JC000611>
- Gallagher, B. (1972). Some qualitative aspects of nonlinear wave radiation in a surf zone. *Geophysical Fluid Dynamics*, 3(4), 347–354. <https://doi.org/10.1080/03091927208236086>
- Gawehn, M., van Dongeren, A., van Rooijen, A., Storlazzi, C. D., Cheriton, O. M., & Reniers, A. (2016). Identification and classification of very low frequency waves on a coral reef flat. *Journal of Geophysical Research: Oceans*, 121(10), 7560–7574. <https://doi.org/10.1002/2016JC011834>
- Goring, D., & Nikora, V. (2002). Despiking acoustic doppler velocimeter data. *Journal of Hydraulic Engineering*, 128(1), 117–126. [https://doi.org/10.1061/\(ASCE\)0733-9429](https://doi.org/10.1061/(ASCE)0733-9429)
- Gourlay, M. R. (1994). Wave transformation on a coral reef. *Coastal Engineering*, 23(1–2), 17–42. [https://doi.org/10.1016/0378-3839\(94\)90013-2](https://doi.org/10.1016/0378-3839(94)90013-2)
- Gourlay, M. R. (1996a). Wave set-up on coral reefs. 1. Set-up and wave-generated flow on an idealised two dimensional horizontal reef. *Coastal Engineering*, 27(3–4), 161–193. [https://doi.org/10.1016/0378-3839\(96\)00008-7](https://doi.org/10.1016/0378-3839(96)00008-7)
- Gourlay, M. R. (1996b). Wave set-up on coral reefs. 2. Set-up on reefs with various profiles. *Coastal Engineering*, 28(1–4), 17–55. [https://doi.org/10.1016/0378-3839\(96\)00009-9](https://doi.org/10.1016/0378-3839(96)00009-9)
- Gourlay, M. R., & Colleter, G. (2005). Wave-generated flow on coral reefs – An analysis for two-dimensional horizontal reef-tops with steep faces. *Coastal Engineering*, 52(4), 353–387. <https://doi.org/10.1016/j.coastaleng.2004.11.007>
- Ha, H. K., Maa, J. P.-Y., Park, K., & Kim, Y. H. (2011). Estimation of high-resolution sediment concentration profiles in bottom boundary layer using pulse-coherent acoustic Doppler current profilers. *Marine Geology*, 279(1), 199–209. <https://doi.org/10.1016/j.margeo.2010.11.002>
- Hardy, T. A., & Young, I. R. (1996). Field study of wave attenuation on an offshore coral reef. *Journal of Geophysical Research*, 101(C6), 14311–14326. <https://doi.org/10.1029/96jc00202>
- Harney, J. N., & Fletcher, C. H. (2003). A budget of carbonate framework and sediment production, Kailua Bay, Oahu, Hawaii. *Journal of Sedimentary Research*, 73(6), 856–868. <https://doi.org/10.1306/051503730856>
- Harris, D. L., Vila-Concejo, A., & Webster, J. M. (2014). Geomorphology and sediment transport on a submerged back-reef sand apron: One Tree Reef, Great Barrier Reef. *Geomorphology*, 222, 132–142. <https://doi.org/10.1016/j.geomorph.2014.03.015>
- Hearn, C. J. (1999). Wave-breaking hydrodynamics within coral reef systems and the effect of changing relative sea level. *Journal of Geophysical Research*, 104, 30007–30019. <https://doi.org/10.1029/1999jc900262>
- Hench, J. L., Leichter, J. J., & Monismith, S. G. (2008). Episodic circulation and exchange in a wave-driven coral reef and lagoon system. *Limnology & Oceanography*, 53(6), 2681–2694. <https://doi.org/10.4319/lo.2008.53.6.2681>
- Hine, A. C., Wilber, R. J., Bane, J. M., Neumann, A. C., & Lorenson, K. R. (1981). Offbank transport of carbonate sands along open, leeward bank margins: Northern Bahamas. *Sedimentary Dynamics of Continental Shelves*, 42(1), 327–348. [https://doi.org/10.1016/0025-3227\(81\)90169-9](https://doi.org/10.1016/0025-3227(81)90169-9)
- Hoegh-Guldberg, O., Pendleton, L., & Kaup, A. (2019). People and the changing nature of coral reefs. *Regional Studies in Marine Science*, 30, 100699. <https://doi.org/10.1016/j.rsma.2019.100699>
- Hsu, T.-J., & Hanes, D. M. (2004). Effects of wave shape on sheet flow sediment transport. *Journal of Geophysical Research*, 109, C05025. <https://doi.org/10.1029/2003JC002075>
- Hughes, T. P. (1999). Off-reef transport of coral fragments at Lizard Island, Australia. *Marine Geology*, 157(1), 1–6. [https://doi.org/10.1016/S0025-3227\(98\)00187-X](https://doi.org/10.1016/S0025-3227(98)00187-X)
- Jago, O., Kench, P. S., & Brander, R. (2007). Field observations of wave-driven water-level gradients across a coral reef flat. *Journal of Geophysical Research*, 112, C06027. <https://doi.org/10.1029/2006JC003740>
- Kench, P. S. (1998a). A currents of removal approach for interpreting carbonate sedimentary processes. *Marine Geology*, 145(3), 197–223. [https://doi.org/10.1016/S0025-3227\(97\)00101-1](https://doi.org/10.1016/S0025-3227(97)00101-1)
- Kench, P. S. (1998b). Physical controls on development of lagoon sand deposits and lagoon infilling in an Indian Ocean atoll. *Journal of Coastal Research*, 14(3), 1014–1024.
- Kennedy, D. M., & Woodroffe, C. D. (2000). Holocene lagoonal sedimentation at the latitudinal limits of reef growth, Lord Howe Island, Tasman Sea. *Marine Geology*, 169(3), 287–304. [https://doi.org/10.1016/S0025-3227\(00\)00093-1](https://doi.org/10.1016/S0025-3227(00)00093-1)
- Larcombe, P., Costen, A., & Woolfe, K. J. (2001). The hydrodynamic and sedimentary setting of nearshore coral reefs, central Great Barrier Reef shelf, Australia: Paluma Shoals, a case study. *Sedimentology*, 48(4), 811–835. <https://doi.org/10.1046/j.1365-3091.2001.00396.x>
- Larcombe, P., Ridd, P. V., Prytz, A., & Wilson, B. (1995). Factors controlling suspended sediment on inner-shelf coral reefs, Townsville, Australia. *Coral Reefs*, 14(3), 163–171. <https://doi.org/10.1007/BF00367235>
- Longuet-Higgins, M. S., & Stewart, R. W. (1964). Radiation stresses in water waves – A physical discussion, with applications. *Deep-Sea Research*, 11(4), 529–562. [https://doi.org/10.1016/0011-7471\(64\)90001-4](https://doi.org/10.1016/0011-7471(64)90001-4)
- Lowe, R. J., Falter, J. L., Bandet, M. D., Pawlak, G., Atkinson, M. J., Monismith, S. G., & Koseff, J. R. (2005). Spectral wave dissipation over a barrier reef. *Journal of Geophysical Research*, 110, C04001. <https://doi.org/10.1029/2004jc002711>
- Lowe, R. J., Falter, J. L., Monismith, S. G., & Atkinson, M. J. (2009a). A numerical study of circulation in a coastal reef-lagoon system. *Journal of Geophysical Research*, 114, C06022. <https://doi.org/10.1029/2008jc005081>
- Lowe, R. J., Falter, J. L., Monismith, S. G., & Atkinson, M. J. (2009b). Wave-driven circulation of a coastal reef-lagoon system. *Journal of Physical Oceanography*, 39, 873–893. <https://doi.org/10.1175/2008JPO3958.1>
- Lugo-Fernández, A., Roberts, H. H., Wiseman, W. J., Jr, & Carter, B. L. (1998). Water level and currents of tidal and infragravity periods at Tague Reef, St. Croix (USVI). *Coral Reefs*, 17(4), 343–349. <https://doi.org/10.1007/s003380050137>
- Malarkey, J., & Davies, A. G. (2012). A simple procedure for calculating the mean and maximum bed stress under wave and current conditions for rough turbulent flow based on Soulsby and Clarke's (2005) method. *Computers and Geosciences*, 43, 101–107. <https://doi.org/10.1016/j.cageo.2012.02.020>
- Marino-Tapia, I. J., Russell, P. E., O'Hare, T. J., Davidson, M. A., & Huntley, D. A. (2007). Cross-shore sediment transport on natural beaches and its relation to sandbar migration patterns: 1. Field observations and derivation of a transport parameterization. *Journal of Geophysical Research*, 112, C3001. <https://doi.org/10.1029/2005JC002893>
- Massel, S. R., & Gourlay, M. R. (2000). On the modelling of wave breaking and set-up on coral reefs. *Coastal Engineering*, 39, 1–27. [https://doi.org/10.1016/S0378-3839\(99\)00052-6](https://doi.org/10.1016/S0378-3839(99)00052-6)
- Mathisen, P. P., & Madsen, O. S. (1999). Waves and currents over a fixed rippled bed 3. Bottom and apparent roughness for spectral waves and currents. *Journal of Geophysical Research*, 104, 18447–18461. <https://doi.org/10.1029/1999jc900114>

- Monismith, S. G., Herdman, L. M. M., Ahmerkamp, S., & Hench, J. L. (2013). Wave transformation and wave-driven flow across a steep coral reef. *Journal of Physical Oceanography*, 43(7), 1356–1379. <https://doi.org/10.1175/JPO-D-12-0164.1>
- Morgan, K. M., & Kench, P. S. (2014). A detrital sediment budget of a Maldivian reef platform. *Geomorphology*, 222, 122–131. <https://doi.org/10.1016/j.geomorph.2014.02.013>
- Morgan, K. M., & Kench, P. S. (2016). Parrotfish erosion underpins reef growth, sand talus development and island building in the Maldives. *Sedimentary Geology*, 341, 50–57. <https://doi.org/10.1016/j.sedgeo.2016.05.011>
- Nakato, T., Kennedy, J. F., Glover, J. R., & Locher, F. A. (1977). Wave entrainment of sediment from rippled beds. *Journal of the Waterway, Port, Coastal and Ocean Division*, 103(1), 83–99.
- Nielsen, P. (1992). *Coastal bottom boundary layers and sediment transport*, Advanced Series on Ocean Engineering, 4, Singapore: World scientific.
- Ogston, A. S., Storlazzi, C. D., Field, M. E., & Presto, M. K. (2004). Sediment resuspension and transport patterns on a fringing reef flat, Molokai, Hawaii. *Coral Reefs*, 23(4), 559–569. <https://doi.org/10.1007/s00338-004-0415-9>
- O'Hara Murray, R. B., Thorne, P. D., & Hodgson, D. (2011). Intrawave observations of sediment entrainment processes above sand ripples under irregular waves. *Journal of Geophysical Research*, 116, C01001. <https://doi.org/10.1029/2010JC006216>
- Péquignat, A.-C. N., Becker, J. M., & Merrifield, M. A. (2014). Energy transfer between wind waves and low-frequency oscillations on a fringing reef, Ipan, Guam. *Journal of Geophysical Research: Oceans*, 119, 6709–6724. <https://doi.org/10.1002/2014JC010179>
- Péquignat, A.-C. N., Becker, J. M., Merrifield, M. A., & Aucan, J. (2009). Forcing of resonant modes on a fringing reef during tropical storm Man-Yi. *Geophysical Research Letters*, 36, L03607. <https://doi.org/10.1029/2008gl036259>
- Perry, C. T., & Hepburn, L. J. (2008). Syn-depositional alteration of coral reef framework through bioerosion, encrustation and cementation: Taphonomic signatures of reef accretion and reef depositional events. *Earth-Science Reviews*, 86(1–4), 106–144. <https://doi.org/10.1016/j.earscirev.2007.08.006>
- Perry, C. T., Kench, P. S., Smithers, S. G., Riegl, B., Yamano, H., & O'Leary, M. J. (2011). Implications of reef ecosystem change for the stability and maintenance of coral reef islands. *Global Change Biology*, 17, 3679–3696. <https://doi.org/10.1111/j.1365-2486.2011.02523.x>
- Pomeroy, A. W. M., Lowe, R. J., Ghisalberti, M., Storlazzi, C., Symonds, G., & Roelvink, D. (2017). Sediment transport in the presence of large reef bottom roughness. *Journal of Geophysical Research: Oceans*, 122(2), 1347–1368. <https://doi.org/10.1002/2016JC011755>
- Pomeroy, A. W. M., Lowe, R. J., Ghisalberti, M., Winter, G., Storlazzi, C., & Cuttler, M. (2018). Spatial variability of sediment transport processes over intratidal and subtidal timescales within a fringing coral reef system. *Journal of Geophysical Research: Earth Surface*, 123(5), 1013–1034. <https://doi.org/10.1002/2017JF004468>
- Pomeroy, A. W. M., Lowe, R. J., Symonds, G., Van Dongeren, A., & Moore, C. (2012). The dynamics of infragravity wave transformation over a fringing reef. *Journal of Geophysical Research*, 117, C11022. <https://doi.org/10.1029/2012JC008310>
- Pomeroy, A. W. M., Lowe, R. J., Van Dongeren, A. R., Ghisalberti, M., Bodde, W., & Roelvink, D. (2015). Spectral wave-driven sediment transport across a fringing reef. *Coastal Engineering*, 98, 78–94. <https://doi.org/10.1016/j.coastaleng.2015.01.005>
- Pomeroy, A. W. M., Van Dongeren, A., Lowe, R. J., de Vries, J. van T., & Roelvink, J. (2012). Low frequency wave resonance in fringing reef environments. *Coastal Engineering Proceedings*, 1(33), 25.
- Presto, M. K., Ogston, A. S., Storlazzi, C. D., & Field, M. E. (2006). Temporal and spatial variability in the flow and dispersal of suspended-sediment on a fringing reef flat, Molokai, Hawaii. *Estuarine, Coastal and Shelf Science*, 67, 67–81. <https://doi.org/10.1016/j.ecss.2005.10.015>
- Roeber, V., & Bricker, J. D. (2015). Destructive tsunami-like wave generated by surf beat over a coral reef during Typhoon Haiyan. *Nature Communications*, 6, 7854. <https://doi.org/10.1038/ncomms8854>
- Rosenberger, K. J., Storlazzi, C. D., Cheriton, O. M., Pomeroy, A. W. M., Hansen, J. E., Lowe, R. J., & Buckley, M. L. (2020). Spectral wave-driven bedload transport across a coral reef flat/lagoon complex. *Frontiers in Marine Science*, 7, 875. <https://doi.org/10.3389/fmars.2020.513020>
- Sanderson, P. G., & Eliot, I. (1996). Shoreline salients, cusped forelands and tombolos on the Coast of Western Australia. *Journal of Coastal Research*, 12(3), 761–773.
- Sleath, J. F. A., & Wallbridge, S. (2002). Pickup from rippled beds in oscillatory flow. *Journal of Waterway, Port, Coastal, and Ocean Engineering*, 128(6), 228–237. [https://doi.org/10.1061/\(ASCE\)0733-950X](https://doi.org/10.1061/(ASCE)0733-950X)
- Soulsby, R. L. (1997). *Dynamics of marine sands: A manual for practical applications*. London: Thomas Telford.
- Soulsby, R. L., & Clarke, S. (2005). *Bed shear-stresses under combined waves and currents on smooth and rough beds*. Produced within Defra Project FD1905 (EstProc).
- Soulsby, R. L., Hamm, L., Klopman, G., Myrhaug, D., Simons, R. R., & Thomas, G. P. (1993). Wave-current interaction within and outside the bottom boundary layer. *Coastal Engineering*, 21(1–3), 41–69. [https://doi.org/10.1016/0378-3839\(93\)90045-a](https://doi.org/10.1016/0378-3839(93)90045-a)
- Sous, D., Tissier, M., Rey, V., Touboul, J., Bouchette, F., Devenon, J.-L., et al. (2019). Wave transformation over a barrier reef. *Continental Shelf Research*, 184, 66–80. <https://doi.org/10.1016/j.csr.2019.07.010>
- Storlazzi, C. D., Field, M. E., & Bothner, M. H. (2010). The use (and misuse) of sediment traps in coral reef environments: Theory, observations, and suggested protocols. *Coral Reefs*, 30, 23–38. <https://doi.org/10.1007/s00338-010-0705-3>
- Storlazzi, C. D., Field, M. E., Bothner, M. H., Presto, M. K., & Draut, A. E. (2009). Sedimentation processes in a coral reef embayment: Hanalei Bay, Kauai. *Marine Geology*, 264, 140–151. <https://doi.org/10.1016/j.margeo.2009.05.002>
- Storlazzi, C. D., & Jaffe, B. E. (2008). The relative contribution of processes driving variability in flow, shear, and turbidity over a fringing coral reef: West Maui, Hawaii. *Estuarine, Coastal and Shelf Science*, 77(4), 549–564. <https://doi.org/10.1016/j.ecss.2007.10.012>
- Storlazzi, C. D., Ogston, A. S., Bothner, M. H., Field, M. E., & Presto, M. K. (2004). Wave- and tidally-driven flow and sediment flux across a fringing coral reef: Southern Molokai, Hawaii. *Continental Shelf Research*, 24(12), 1397–1419. <https://doi.org/10.1016/j.csr.2004.02.010>
- Suhayda, J. N., & Roberts, H. H. (1977). *Wave action and sediment transport on fringing reefs*. Presented at the 3rd International Coral Reef Symposium.
- Symonds, G., Black, K. P., & Young, I. R. (1995). Wave-driven flow over shallow reefs. *Journal of Geophysical Research*, 100, 2639–2648. <https://doi.org/10.1029/94jc02736>
- Symonds, G., Huntley, D. A., & Bowen, A. J. (1982). Two dimensional surfbeat: Long wave generation by a time varying breakpoint. *Journal of Geophysical Research*, 87, 492–498. <https://doi.org/10.1029/JC087iC01p00492>
- Taebi, S., Lowe, R. J., Pattiaratchi, C. B., Ivey, G. N., Symonds, G., & Brinkman, R. (2011). Nearshore circulation in a tropical fringing reef system. *Journal of Geophysical Research*, 116, C02016. <https://doi.org/10.1029/2010jc006439>
- Terrile, E., Reniers, A. J. H. M., Stive, M. J. F., Tromp, M., & Verhagen, H. J. (2006). Incipient motion of coarse particles under regular shoaling waves. *Coastal Engineering*, 53(1), 81–92. <https://doi.org/10.1016/j.coastaleng.2005.08.004>

- Thorne, P. D. (2002). Suspended sediments under waves measured in a large-scale flume facility. *Journal of Geophysical Research*, *107*(C8), <https://doi.org/10.1029/2001JC000988>
- Thorne, P. D., Davies, A. G., & Bell, P. S. (2009). Observations and analysis of sediment diffusivity profiles over sandy rippled beds under waves. *Journal of Geophysical Research: Oceans*, *114*, C02023. <https://doi.org/10.1029/2008JC004944>
- van der Werf, J. J., van der, J. S., Doucette, T., & Ribberink, J. S. (2007). Detailed measurements of velocities and suspended sand concentrations over full-scale ripples in regular oscillatory flow. *Journal of Geophysical Research: Earth Surface*, *112*, F02012. <https://doi.org/10.1029/2006JF000614>
- Van Dongeren, A., Lowe, R., Pomeroy, A. W. M., Trang, D. M., Roelvink, D., Symonds, G., & Ranasinghe, R. (2013). Numerical modeling of low-frequency wave dynamics over a fringing coral reef. *Coastal Engineering*, *73*, 178–190. <https://doi.org/10.1016/j.coastaleng.2012.11.004>
- Vetter, O., Becker, J. M., Merrifield, M. A., Pequignet, A.-C., Aucan, J., Boc, S. J., & Pollock, C. E. (2010). Wave setup over a Pacific Island fringing reef. *Journal of Geophysical Research*, *115*, C12066. <https://doi.org/10.1029/2010JC006455>
- Vila-Concejo, A., Harris, D. L., Power, H. E., Shannon, A. M., & Webster, J. M. (2014). Sediment transport and mixing depth on a coral reef sand apron. *Geomorphology*, *222*, 143–150. <https://doi.org/10.1016/j.geomorph.2013.09.034>
- Woodroffe, C. D., McLean, R. F., Smithers, S. G., & Lawson, E. M. (1999). Atoll reef-island formation and response to sea-level change: West Island, Cocos (Keeling) Islands. *Marine Geology*, *160*(1), 85–104. [https://doi.org/10.1016/S0025-3227\(99\)00009-2](https://doi.org/10.1016/S0025-3227(99)00009-2)
- Yahel, R., Yahel, G., & Genin, A. (2002). Daily cycles of suspended sand at coral reefs: A biological control. *Limnology and Oceanography*, *47*(4), 1071–1083. <https://doi.org/10.4319/lo.2002.47.4.1071>